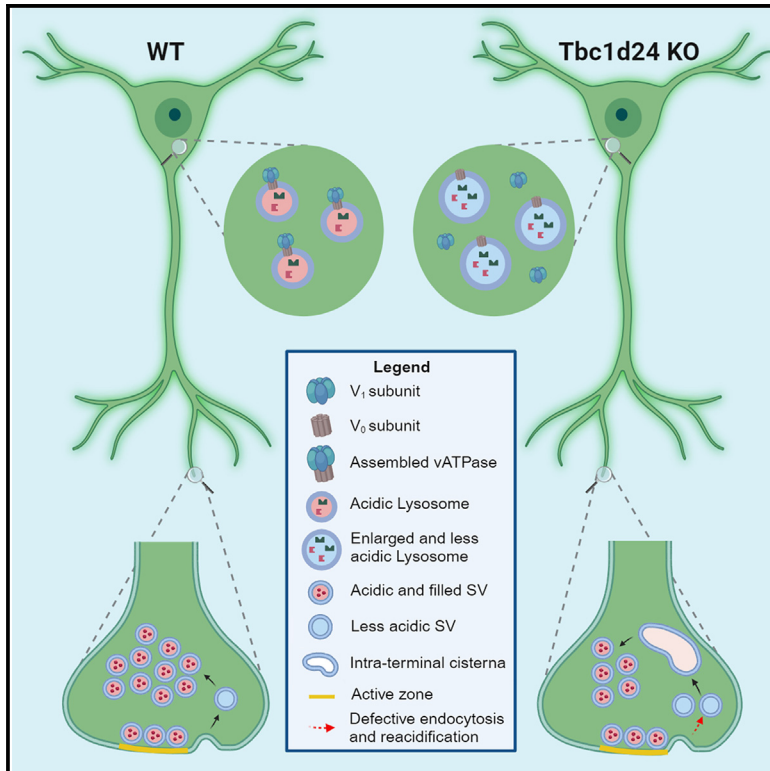


TBC1D24 interacts with the v-ATPase and regulates intraorganellar pH in neurons

Graphical abstract



Authors

Sara Pepe, Davide Aprile, Enrico Castroflorio, ..., Fabio Benfenati, Peter L. Oliver, Anna Fassio

Correspondence

afassio@unige.it

In brief

Molecular neuroscience; Cellular neuroscience

Highlights

- TBC1D24 interacts with the v-ATPase in neurons
- Defective v-ATPase assembly occurs in *Tbc1d24* knockout neurons
- *Tbc1d24* knockout neurons show disrupted lysosomal acidification and autophagy
- Impaired synaptic vesicle recycling and reacidification occurs at *Tbc1d24* knockout synapses



Article

TBC1D24 interacts with the v-ATPase and regulates intraorganellar pH in neurons

Sara Pepe,^{1,2} Davide Aprile,^{1,5} Enrico Castroflorio,³ Antonella Marte,¹ Simone Giubbolini,¹ Samir Hopestone,³ Anna Parsons,³ Tânia Soares,³ Fabio Benfenati,^{2,4} Peter L. Oliver,³ and Anna Fassio^{1,2,6,*}

¹Department of Experimental Medicine, University of Genova, Viale Benedetto XV/3, 16132 Genoa, Italy

²IRCCS Ospedale Policlinico San Martino, Largo Rosanna Benzi 10, 16132 Genoa, Italy

³MRC Mammalian Genetics Unit, MRC Harwell Institute, Harwell Campus, Didcot, OX11 0RD, UK

⁴Center for Synaptic Neuroscience and Technology, Istituto Italiano di Tecnologia, Largo Rosanna Benzi 10, 16132 Genoa, Italy

⁵Human Technopole, Viale Rita Levi-Montalcini 1, 20157 Milan, Italy

⁶Lead contact

*Correspondence: afassio@unige.it

<https://doi.org/10.1016/j.isci.2024.111515>

SUMMARY

The vacuolar ATPase (v-ATPase) is essential for acidification of intracellular organelles, including synaptic vesicles. Its activity is controlled by cycles of association and dissociation of the ATP hydrolysis (V_1) and proton transport (V_0) multi-protein subunits. Mutations in genes coding for both v-ATPase subunits and TBC1D24 cause neurodevelopmental disorders with overlapping syndromes; therefore, it is important to investigate their potentially interrelated functions. Here, we reveal that TBC1D24 interacts with the v-ATPase in the brain. Using a constitutive *Tbc1d24* knockout mouse model, we observed accumulation of lysosomes and non-degraded lipid materials in neuronal tissue. In *Tbc1d24* knockout neurons, we detected V_1 mis-localization with increased pH at endo-lysosomal compartments and autophagy impairment. Furthermore, synaptic vesicles endocytosis and reacidification were impaired. Thus, we demonstrate that TBC1D24 is a positive regulator of v-ATPase activity in neurons suggesting that alteration of pH homeostasis could underlie disorders associated with TBC1D24 and the v-ATPase.

INTRODUCTION

The internal pH of cellular compartments is a dynamic and tunable feature of their functionality, modulating fundamental processes that range from lysosomal enzyme degradation and endosomal recycling to the optimization of neurotransmitter loading by synaptic vesicles (SVs). The multi-subunit vacuolar ATPase (v-ATPase) acts as an essential regulator of organelle pH homeostasis in eukaryotes by facilitating the active, ATP-dependent translocation of protons. The v-ATPase complex comprises a cytoplasmic (V_1) domain containing the ATP catalytic site and a membrane (V_0) domain that facilitates hydrogen ion transport by rotary action. In recent years, significant progress has been made regarding the evolutionary conservation and the structural and kinetic properties of this complex, whereby the diversity of v-ATPase subunit composition can drive tissue and organelle-specific activity. The atomic structure of the mammalian brain v-ATPase has been recently resolved, showing that the ATP6AP1 and ATP6AP2 subunits act as assembly factors for the V_0 domain.¹ The reversible assembly/disassembly of the v-ATPase domains is therefore a fundamental regulatory mechanism, yet it is still unclear how this process is precisely controlled in specific cell types such as neurons. At the synapse, V_1/V_0 disassembly has been reported to allow SV fusion and regulate availability of SVs for release.² The assembled V_1/V_0 ho-

loenzyme has been detected on clathrin-coated endocytosed vesicles, where clathrin blocks v-ATPase activity and prevents acidification before uncoating.³

The essential role of v-ATPase in the nervous system is illustrated by the numerous pathogenic mutations in V_1 and V_0 subunits that cause a range of primarily neurodevelopmental disorders.^{4–8} For example, recent studies on *de novo* heterozygous variants of v-ATPase V_1 subunit A (*ATP6V1A*) revealed a spectrum of severe clinical phenotypes, including childhood-onset seizures and progressive neurodegeneration. Cellular and structural modeling experiments suggested a catalytic or stability-driven loss-of-function mechanism for many of the mutations, although hyper-acidification was observed for two variants that were responsible for milder clinical outcomes.^{4,8} Similarly, the V_1 B2 subunit (*ATP6V1B2*) is the site of pathogenic variants responsible for rare neurodevelopmental disorders, including autosomal dominant deafness onychodystrophy (DDOD) and some cases of deafness onychodystrophy osteodystrophy mental retardation and seizures (DOORS) syndrome.^{9,10} Initial functional data have suggested that defective organelle acidification may underlie certain *ATP6V1B2* heterozygous truncation mutations.¹¹ Intriguingly, the very rare and specific combination of clinical features in DOORS syndrome is shared by biallelic variants in the Tre2–Bub2–Cdc16 (TBC1) domain-containing Family Member 24 (*TBC1D24*) gene,¹² suggesting that there may be



interconnected etiological mechanisms, although this has not been functionally investigated as yet.

Since the advent of exome sequencing and genetic screening panels, an increasing number of *TBC1D24* pathogenic variants – now numbering over 80 – have been identified in neurological diseases.^{13,14} Childhood-onset epileptic seizures are common, including variants of myoclonic epilepsy and epileptic encephalopathy, with some cases refractory to treatment. Additionally, reported clinical features include neurodevelopmental delay, neurodegeneration, and non-syndromic hearing loss. Almost all *TBC1D24* pathogenic mutations are recessive or compound heterozygous, with examples of protein instability and premature termination sequences supporting a loss-of-function mode of action. Primary neurons from mice modeling *Tbc1d24* haploinsufficiency show an enlarged endosomal compartment, reminiscent of the endosomal vesicle accumulation observed in *Drosophila skywalker* mutants used to model conserved DOORS variants.^{15,16} Interestingly, recessive mutations in the related gene oxidation resistance 1 (*OXR1*) have since been described; patients display pediatric seizures and cerebellar neurodegeneration with some pathological evidence in *Drosophila* and human fibroblasts that lysosomal dysfunction occurs as a result of *OXR1* loss.¹⁷ Both genes harbor a highly conserved C-terminal TLDc domain and recent *in vitro* and structural studies have proposed that TLDc proteins interact with v-ATPase with different affinity.¹⁸ However, how TLDc proteins regulate v-ATPase stability and/or assembly state *in vivo* is not known, as well as the pathophysiological role of impaired interactions with v-ATPase in the context of neurodevelopmental disorders associated with *TBC1D24* mutations.

Therefore, the aim of this study was to understand the impact of *TBC1D24* loss-of-function on v-ATPase activity in the nervous system and to define the effects on endo-lysosomal pathology alongside organelle and SV acidification. Combining cellular and *in vivo* studies of a *Tbc1d24* null mouse mutant introduced here, we reveal that *Tbc1d24* interacts with V1 subunits of the v-ATPase in the brain and that loss of *Tbc1d24* expression results in increased pH at intracellular compartments and autophagy impairment in neurons. *Tbc1d24*-depleted synapses display decreased SV density, accumulation of degradative vacuoles and impaired SV acidification. We propose *TBC1D24* as a neuronal regulator of v-ATPase assembly and dysregulation of neuronal pH homeostasis as a common feature for neurodevelopmental disorders associated with *TBC1D24* and v-ATPase subunit variants.

RESULT

TBC1D24 interacts with v-ATPase in the brain

TBC1D24 has been reported to interact with v-ATPase in the kidney and to preferentially co-immunoprecipitate with the kidney-specific ATP6V1B1 subunit.¹⁸ To assess if the *TBC1D24*:v-ATPase interaction occurs with the ATP6V1B2 subunit, that is highly expressed in the brain,^{1,19} we performed pull-down experiments in COS-7 cells expressing a 3xFLAG-tagged form of human *TBC1D24* (FLAG-*TBC1D24*), using a 3xFLAG empty vector (FLAG) and a 3xFLAG-tagged bacterial alkaline phosphate (FLAG-BAP) as negative controls. Comparable amounts of

FLAG-*TBC1D24* and FLAG-BAP were detected in the input samples at the expected molecular masses (70kDa and 55kDa, respectively) and both efficiently co-precipitated in the pull-down samples (Figure 1A). We revealed the selective pull-down of endogenous ATP6V1B2 and its molecular partner ATP6V1A by FLAG-*TBC1D24* with no detectable immunoreactive bands in the FLAG and FLAG-BAP controls (Figure 1A). To further confirm those interactions, we performed co-immunoprecipitation experiments in COS-7 cells overexpressing either FLAG-*TBC1D24* or FLAG-BAP together with either human HA-tagged ATP6V1B2 (ATP6V1B2-HA) or untagged ATP6V1A; the targets were also co-expressed with untagged *TBC1D24* as a control. These data confirmed the specific interaction of *TBC1D24* with the two main subunits of the V1 domain of brain v-ATPase with no detectable immunoreactivity in the negative control FLAG-BAP samples (Figures S1A and S1B). We next investigated whether these interactions occur endogenously in brain tissue, by performing immunoprecipitation experiments from mouse brain lysates where we were able to detect a significant co-immunoprecipitation of both Atp6v1b2 and Atp6v1a by anti-*TBC1D24* antibodies but not with non-specific IgG antibodies (Figures 1B and S1C).

To further corroborate these data, we analyzed the localization of *TBC1D24* and ATP6V1B2 in neurons; we overexpressed mCherry-tagged *TBC1D24* (*TBC1D24*-mCherry) and GFP-tagged ATP6V1B2 (ATP6V1B2-eGFP) in mouse hippocampal primary neurons at 12 days *in vitro* (12 DIV) and analyzed the fluorescent signals two days later. The overexpressed proteins showed a high and significant degree of colocalization both at cell soma and along neurites (Figure 1C). Overall, these data show that *TBC1D24* interacts with V1 subunits of the v-ATPase complex in the brain and colocalizes with ATP6V1B2 at subcellular level in neurons.

Tbc1d24 loss results in perinatal lethality and accumulation of aberrant lysosomes in brain tissue

To determine the *in vivo* significance of the *TBC1D24*:v-ATPase interaction in the brain, we generated a *Tbc1d24* null mouse model (KO) by CRISPR/Cas9 targeting, which led to a stably inherited two-nucleotide insertion in exon 3 of *Tbc1d24*, resulting in a predicted frameshift at amino acid 137 and premature stop at codon 182 (Figure 2A). From assessing the first intercross litters it was apparent that homozygous KO pups died at, or very soon after birth, however pathological analysis at late embryonic stages (E18.5) revealed no abnormal gross brain structural alterations (Figure 2B). To confirm that the mutant insertion generated a true null allele of *Tbc1d24*, expression studies of late embryonic brain tissue were carried out. Quantitative (q)RT-PCR showed that the mutant transcript was expressed at approximately half that of the wild-type (WT), and this was confirmed by *in situ* hybridization on E16.5 brain sections (Figures 2C and 2D). Nevertheless, western blotting confirmed a complete loss of full-length *Tbc1d24* protein in KO animals, with an approximate 50% reduction in the HET E18.5 brain (Figures 2E and 2F). Together, these data show that total loss of the *Tbc1d24* protein *in vivo* is not viable in mice.

Despite no gross brain structural abnormalities in KO embryos, we analyzed whether loss of *Tbc1d24* affected organelle

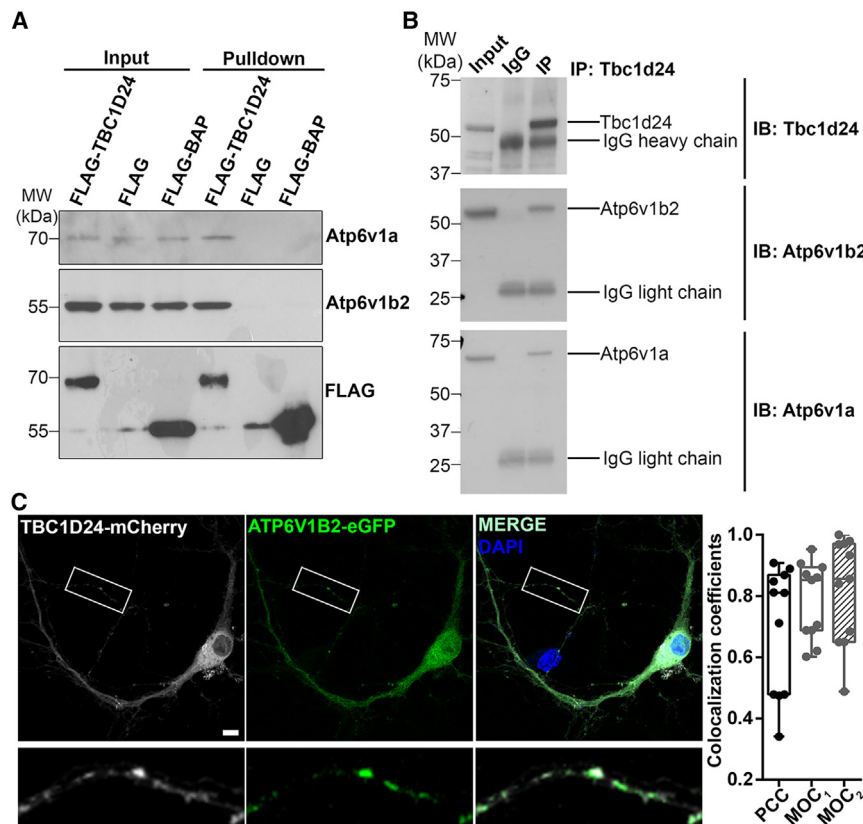


Figure 1. Tbc1d24 interacts with v-ATPase in brain cells

(A) Western blotting for Atp6v1a, Atp6v1b2 and FLAG in COS-7 cells lysates (Input) and pull-down with FLAG-tagged resins (Pull-down). COS-7 cells were transfected with 3xFLAG-Tbc1D24 (FLAG-Tbc1D24), empty vector (FLAG) and 3xFLAG-BAP (FLAG-BAP).

(B) Western blotting for Atp6v1a and Atp6v1b2 in total mouse brain lysates (Input) and immunoprecipitated with IgG (IgG) and anti-Tbc1D24 antibodies (IP).

(C) *Left*: representative images of primary neurons transfected with Tbc1D24-mCherry and ATP6V1B2-eGFP and analyzed at 14 DIV. White rectangles indicate regions shown at high magnification below. Scale bar, 10 μ m. *Right*: Pearson correlation coefficient (POC) and Manders' overlap coefficients (MOC1: Tbc1D24 overlapping with ATP6V1B2 and MOC2: ATP6V1B2 overlapping with Tbc1D24). Boxplots (center line, median [Q2]; box limits, 25th [Q1]-75th [Q3] percentiles; whisker length, the outermost data points within 3-fold the interquartile range [Q3-Q1]) of 11 neurons for experimental group from two independent preparations.

distribution and synaptic ultrastructure, as suggested by previous studies.^{15,20} Initially, we analyzed neuronal ultrastructure by electron microscopy at late embryonic stages (E18.5), revealing enlarged lysosomes at the soma of KO neurons with a significant increase in the mean lysosomal area compared to the WT. This phenotype was accompanied by an accumulation of lipid droplets, which was virtually absent in WT brains (Figure 3A). Considering the already reported presynaptic role for Tbc1d24,^{15,21} we evaluated the synaptic ultrastructure in E18.5 brain tissue, and revealed a significant accumulation of cisternae-like structures together with decreased SV density in neurons from KO mice compared to the WT (Figure 3B). The data suggest alteration in lysosomal and synaptic compartments upon chronic Tbc1d24 loss.

Tbc1d24 loss results in cytosolic shift of the v-ATPase V1 domain and increased intra-organelle pH in neurons

Since the E18.5 mouse brain is highly immature and characterized by developing neurons and ongoing synaptogenesis, we employed primary neurons from KO embryos for further mechanistic and pathological studies in neuronal cells. We first evaluated the effects of the constitutive loss of Tbc1d24 on neuronal v-ATPase activity and intracellular organelle acidification. The regulation of v-ATPase activity predominantly occurs by controlling the reversible association of the V₁ and V₀ domains. Thus, we investigated if the lack of Tbc1d24 could affect the assembly state of the v-ATPase complex. Protein expression of v-ATPase subunits either belonging to the cytosolic V₁ domain (Atp6v1a

and Atp6v1b2) or to the transmembrane V₀ domain (Atp6v0a1), was not different in total cellular lysates from WT and KO primary cortical neurons (Figure 4A). However, the subcellular fractionation of cytosolic and membrane proteins revealed a significant increase in the amount of cytosolic Atp6v1a and Atp6v1b2 in KO compared to WT cortical neurons, paired with a significant reduction in the membrane localization of both subunits (Figure 4B). No changes were detected for Atp6v0a1, which was only detectable and similarly expressed in the membrane fraction of both WT and KO samples (Figure 4B). These data point to a potential shift in v-ATPase assembly, not associated with changes in expression, when Tbc1d24 is deleted constitutively.

We also examined two further aspects that support a role for Tbc1D24 in v-ATPase functionality. v-ATPase targeting activity is regulated by phosphatidylinositol phosphate lipids (PIPs) in yeast and mammals²²; in addition, the *Drosophila* homologue of Tbc1D24, *skywalker*, was reported to contain a lipid pocket domain.¹⁶ Interestingly, we show preferential binding of Tbc1D24 for PI(3)P, PI(5)P, PI(3,5)P2 and PI(4,5)P2, lipids typically enriched in endosomes and lysosomes (Figure S2A). Furthermore, v-ATPase has been reported to specifically interact with Arf6 and its regulator ARNO to promote Arf6 activation.²³ Interestingly, we here reveal that Tbc1d24 chronic deletion resulted in increased levels of GTP-bound Arf6, as revealed by GGA3 pull-down from WT and KO neuronal lysates (Figure S2B) and previously reported in acute knockdown models.²⁴

We next investigated whether loss of Tbc1d24 could alter intracellular organelle distribution and acidification. We performed quantitative image analysis to measure LysoTracker signal in hippocampal neurons at 12–14 DIV and we found that KO cells

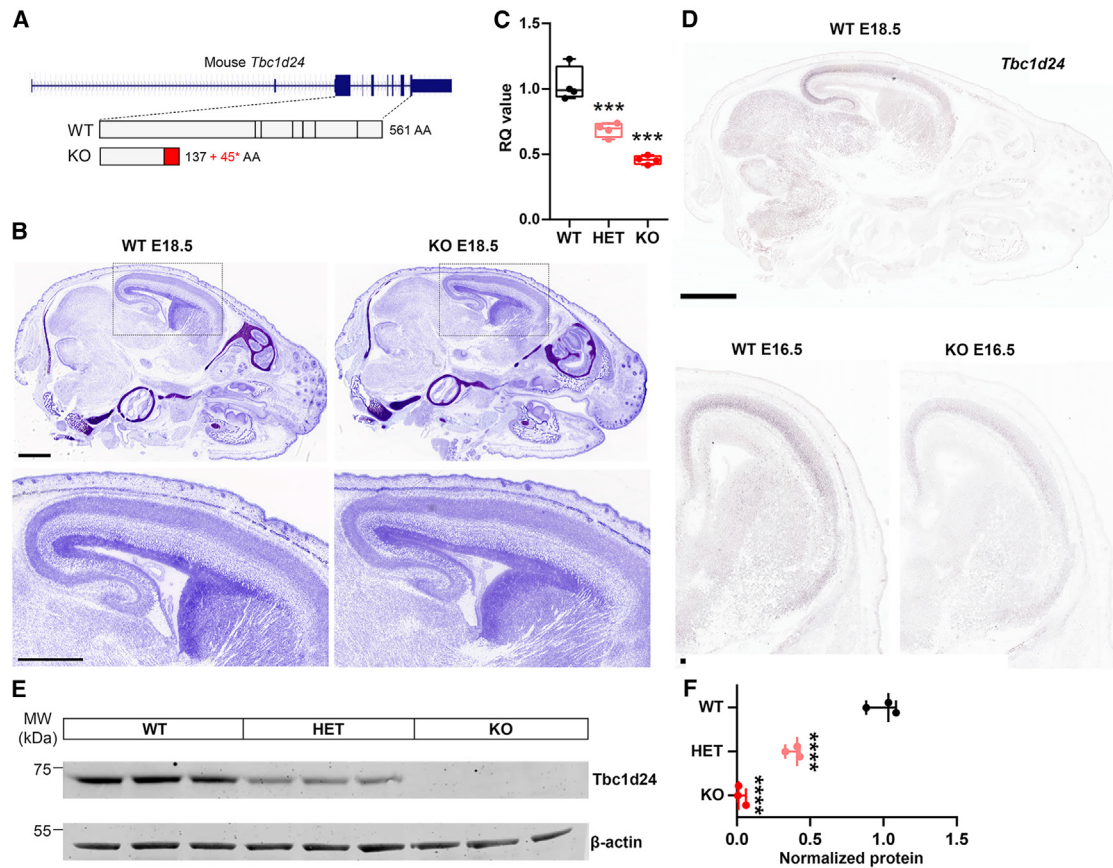


Figure 2. *Tbc1d24* KO mouse model

(A) Scheme of mouse *Tbc1d24* intron/exon structure and corresponding proteins. The KO allele contains two nucleotide insertion resulting in a predicted truncated protein.
 (B) Nissl staining of E18.5 heads from WT and KO mice. Higher magnification in lower panels as indicated. Scale bar, 0.5 mm.
 (C) Quantitative qPCR for *Tbc1d24* from E16.5 cortical brain tissue for WT, KO and heterozygous (HET) mice; Boxplots (center line, median [Q2]; box limits, 25th [Q1]-75th [Q3] percentiles; whisker length, the outermost data points within 3-fold the interquartile range [Q3-Q1]) of 4 replications, *** $p < 0.001$, one-way ANOVA vs. WT.
 (D) *In situ* hybridization of *Tbc1d24* in WT E18.5 heads and coronal brain sections at E16.5 from both genotypes. Scale bar, 0.5 mm.
 (E and F) Western blotting of *Tbc1d24* from E18.5 cortical brain tissue (E) and quantification (F); Plots represent median, maximum and minimum of 3 replications for experimental groups. **** $p < 0.0001$, one-way ANOVA/Dunnett's tests vs. WT.

displayed both a significant decrease in signal intensity and a reduction in the number of LysoTracker-positive puncta with respect to WT neurons at the cell soma (Figure 5A). This phenotype was completely rescued when exogenous human-TBC1D24 was reintroduced in KO neurons, while no effects were observed in WT cells (Figure 5A). To discriminate whether the decrease in LysoTracker staining was due to an increased pH or a lower abundance of intracellular acidic organelles, we performed live imaging experiments with the ratiometric probe LysoSensor yellow/blue DND-160. KO neurons displayed a significantly higher ratio of LysoSensor yellow/blue staining compared to WT, indicative of increased endo-lysosomal pH (Figure 5B). In addition, immunostaining of endogenous Lamp1 at neuronal cell bodies revealed an increase in the intensity and number of immunoreactive puncta in KO neurons compared to the WT (Figure 5C). This accumulation of Lamp1-positive structures was also confirmed by western blotting analysis in cellular lysates from 12 DIV cortical neurons, with a significant increase in KO lysates (Figure 5C). These findings were

supported by *Tbc1d24* acute knockdown experiments in rat hippocampal neurons transduced with a short hairpin RNA (Sh-TBC) that showed decreased LysoTracker signal together with increased Lamp1 staining compared to cultures infected with the scramble control (Scr-TBC) and both phenotypes were efficiently rescued by the overexpression of exogenous TBC1D24 (Figures S3A and S3B). Consistently, TBC1D24 signal partially overlapped with lysosomal Lamp1 marker in neuronal cultures, in particular at the level of cell soma (Figures S3C and S3D). Taken together, these data support the hypothesis that loss of *Tbc1d24* leads to an impairment in the acidification of intracellular endo-lysosomal organelles and accumulation of aberrant Lamp1-positive structures at the neuronal soma.

Tbc1d24 loss results in autophagy impairment in neurons and synapses

Correct acidification of Lamp1-positive lysosomes is necessary for the progression of autophagy, a degradative process

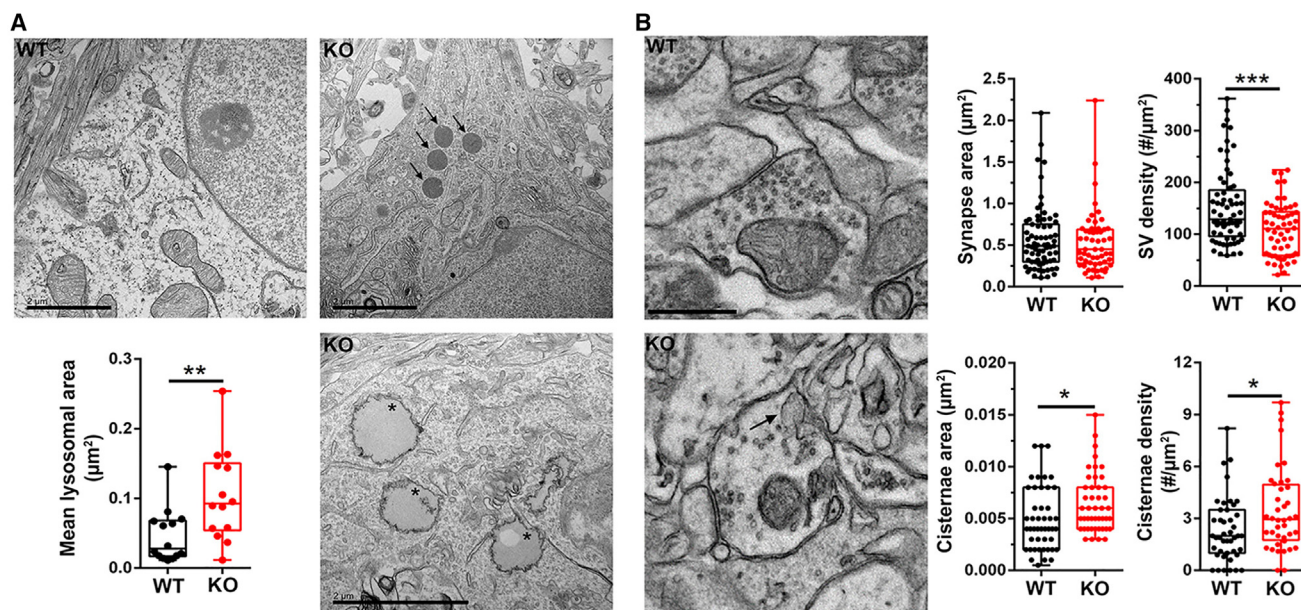


Figure 3. Lysosomal and synaptic abnormalities in *Tbc1d24* KO brains

(A) Electron microscopy images of E18.5 WT and KO brain sections at the neuronal soma. Arrows indicate enlarged lysosomes and asterisks indicate lipid droplets. Boxplots (center line, median [Q2]; box limits, 25th [Q1]-75th [Q3] percentiles; whisker length, the outermost data points within 3-fold the interquartile range [Q3-Q1]) of 14 sections for experimental group. $n = 46$ (WT) and $n = 35$ (KO) lysosomes were measured for experimental group. $**p \leq 0.01$, Mann-Whitney U-test. Scale bars, 2 μm .

(B) *Left*: Electron microscopy images of E18.5 WT and KO brain sections showing synaptic contacts. Arrow indicates enlarged vesicle (cisterna). *Right*: Boxplots (center line, median [Q2]; box limits, 25th [Q1]-75th [Q3] percentiles; whisker length, the outermost data points within 3-fold the interquartile range [Q3-Q1]) of the synaptic area, SV density, cisternae area and density. Data are from $n = 43$ -71 (WT) and $n = 40$ -58 (KO) synapses for experimental group. $*p < 0.05$, $***p < 0.001$, unpaired Student's *t* test/Mann-Whitney U-test. Scale bar, 0.5 μm .

fundamental for neuronal protein homeostasis and synaptic function.²⁵⁻²⁷ To address a potential perturbation of autophagy in *Tbc1d24* KO neurons, we analyzed the expression of the autophagy receptor p62 and the autophagosomal associated protein LC3. Immunocytochemistry experiments and quantification of somatic LC3 and p62, show an increased fluorescent signal in KO hippocampal neurons suggesting defective autophagic clearance upon *Tbc1d24* loss (Figure 6A). Western blotting analysis confirmed significant increased signals for p62 and LC3-II in KO cortical neurons compared to WT (Figure 6B).

TBC1D24 is known to be expressed at synaptic sites^{20,28} and to play a role in SV and receptor recycling.^{15,20} By tissue fractionation techniques, here we confirmed enrichment of *Tbc1d24* expression in purified synaptosomes from WT rat cerebral cortex. As expected, *Atp6v1a* and *Atp6v1b2* expression was also increased in the synaptosomal fraction, due to their high level of expression of the subunits in SVs^{1,29} (Figure S4A). Colocalization experiments with glutamatergic synaptic markers vGlut-1 and Homer1 suggested that, as previously reported,^{20,28} TBC1D24 is expressed at both presynaptic and postsynaptic sites (Figures S4B and S4C). Differential extraction of synaptosomal proteins revealed that *Tbc1d24* is associated with post-synaptic and presynaptic membranes (Figure S4D).

We therefore evaluated autophagy at presynaptic sites in WT and KO primary neurons, employing the FU-Syp-mCh-P2A-eGFP-LC3 lentiviral construct that by co-expressing mCherry-tagged Synaptophysin (Syp-mCh) and eGFP-tagged LC3

(eGFP-LC3) allows to visualize presynaptic autophagic structures.³⁰ Hippocampal neurons were transduced with FU-Syp-mCh-P2A-eGFP-LC3 at 14 DIV and analyzed for LC3/Syp expression at 17-18 DIV. Quantitative image analysis revealed a larger number of double-positive eGFP-LC3/Syp-mCherry puncta in KO neurons, alongside an increased intensity of the eGFP-LC3 signal in Syp-mCherry-positive puncta (Figure 6C). These data are consistent with an accumulation of LC3-positive structures at presynaptic terminals upon *Tbc1d24* deletion.

***Tbc1d24* loss results in altered synaptic ultrastructure and impaired synaptic vesicle endocytosis and reacidification at hippocampal synapses**

To investigate in detail the morphological features of presynaptic terminals lacking *Tbc1d24*, we performed transmission electron microscopy (TEM) acquisition on serial sections from KO and WT primary cortical neurons at 17 DIV, followed by three-dimensional reconstruction. Ultrastructural analysis revealed a significant decrease in the total number of SVs per synapse, but with no changes in the number of docked SVs. In addition, KO synapses displayed an accumulation of intra-terminal cisternae which increased in number and volume (Figures 7A and 7B).

In parallel, to better clarify the impact of *Tbc1d24* loss on v-ATPase subunits, endo-lysosomal and autophagic markers expression at the synaptic boutons, we performed western blotting analysis on total homogenate and synaptic terminal-enriched fractions from primary WT and KO cortical neurons. We

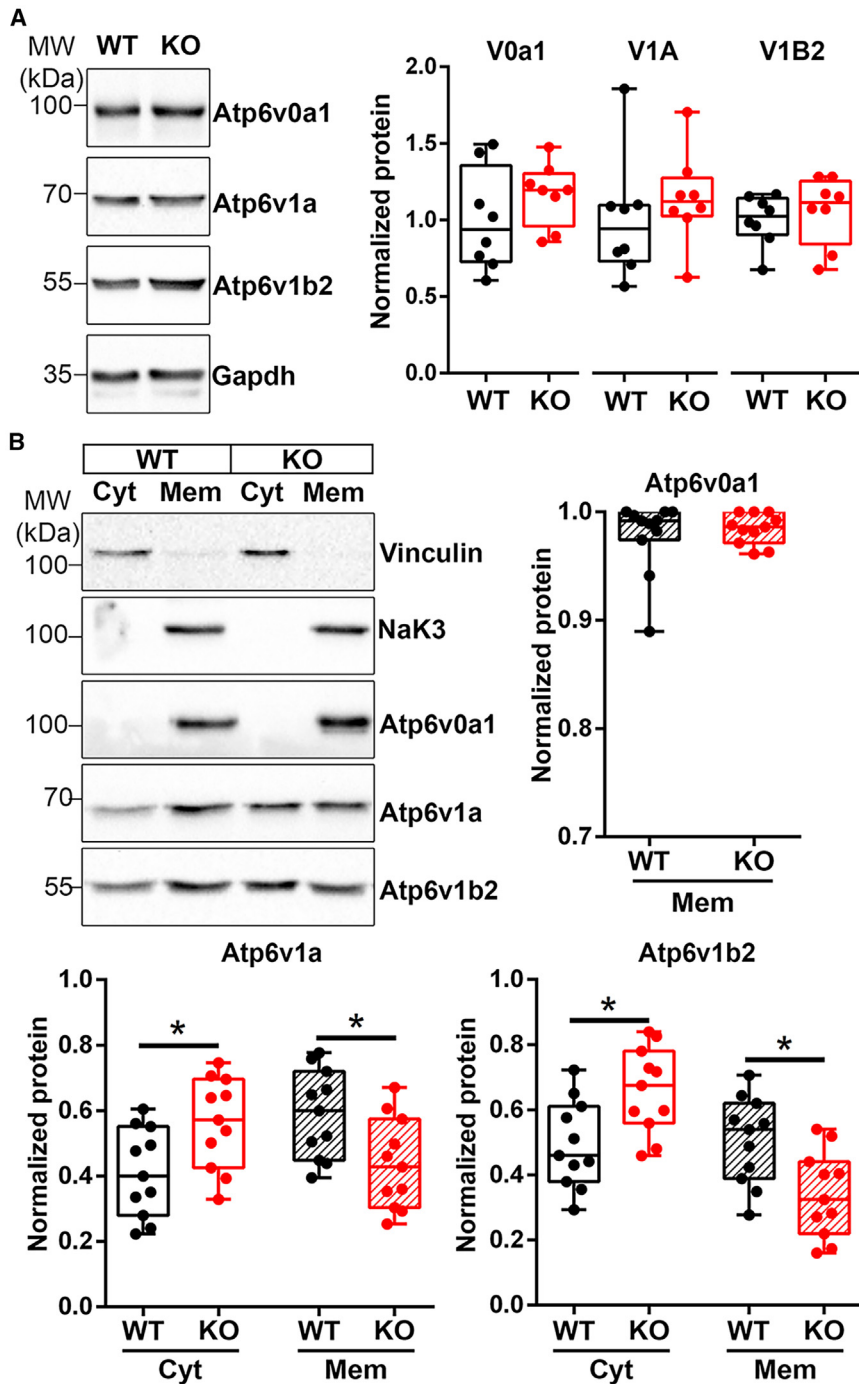


Figure 4. Tbc1d24 KO neurons display a cytosolic shift of V₁ subunits

(A) *Left*: Representative Western blotting of Atp6v0a1, Atp6v1a and Atp6v1b2 subunits and Gapdh as loading control, from WT and KO cortical neurons (12 DIV); *Right*: Densitometric analysis of Atp6v0a1, Atp6v1a and Atp6v1b2 signals normalized on Gapdh and expressed as percentage of WT. Boxplots (center line, median [Q2]; box limits, 25th [Q1]-75th [Q3] percentiles; whisker length, the outermost data points within 3-fold the interquartile range [Q3-Q1]) of 8 replications. Each dot represents lysate from a single embryo.

(B) *Upper left*: Representative Western blotting of Atp6v0a1, Atp6v1a and Atp6v1b2 subunits from cytosolic (Cyt) and membrane (Mem) fractions from neuronal lysates as in A. Vinculin and NaK3 signals were used as cytosolic and membrane markers, respectively. *Upper right and Bottom*: Densitometric analysis of Atp6v0a1, Atp6v1a and Atp6v1b2 signals. Cytosolic fractions were normalized to Vinculin and membrane fractions to NaK3. Data are expressed as percentage of total protein. Boxplots (center line, median [Q2]; box limits, 25th [Q1]-75th [Q3] percentiles; whisker length, the outermost data points within 3-fold the interquartile range [Q3-Q1]) of 11 replications. Each dot represents Cyt or Mem fraction from neuronal cells prepared from a single embryo. **p* < 0.05, one-way ANOVA, Sidak's multiple comparisons test.

cant increase in LC3-II signal together with increased amounts of Rab7 and Lamp1, which were barely detectable in the less loaded synaptosomal samples, at KO terminals with respect to WT (Figure 7D). These data suggest that KO terminals express higher endosomal-lysosomal and autophagy markers compared to WT.

To investigate if these lysosomal and autophagic alterations finally resulted in pH dysregulation in SVs, we transduced 14 DIV primary hippocampal neurons with the genetically encoded reporter synaptophysin-pHluorin (SypHy) and performed live imaging analysis at 18–19 DIV. We first titrated SypHy fluorescence at fixed pH values and obtained a calibration curve for the measurement of

observed a similar enrichment of SV and plasma membrane presynaptic proteins (Syp and Snap25) as well as of members of the v-ATPase complex (Atp6v0a1, Atp6v1a, Atp6v1b2) (Figure 7C). When analyzing early endosome (Rab5) and autophagic (LC3/II) markers, we only revealed a slight but not significant enrichment for LC3-II at KO terminals with respect to WT (Figure 7C). Loading a higher amount of the synaptosomal fractions, to better detect and compare protein expression, we revealed a signifi-

intrasympaptic pH (Figure S5A). To evaluate SV pH at rest, neurons were perfused with Tyrode's solution to measure the basal fluorescence (F₀), then with MES buffer to measure the fluorescence after quenching of the membrane stranded SypHy (F_Q). Neurons were then stimulated with 50 mM KCl to induce SV release and recycling and exposed to a second quenching, to measure SypHy that did not recover after stimulation. NH₄Cl was perfused at the end of the time lapse to evaluate the total amount of

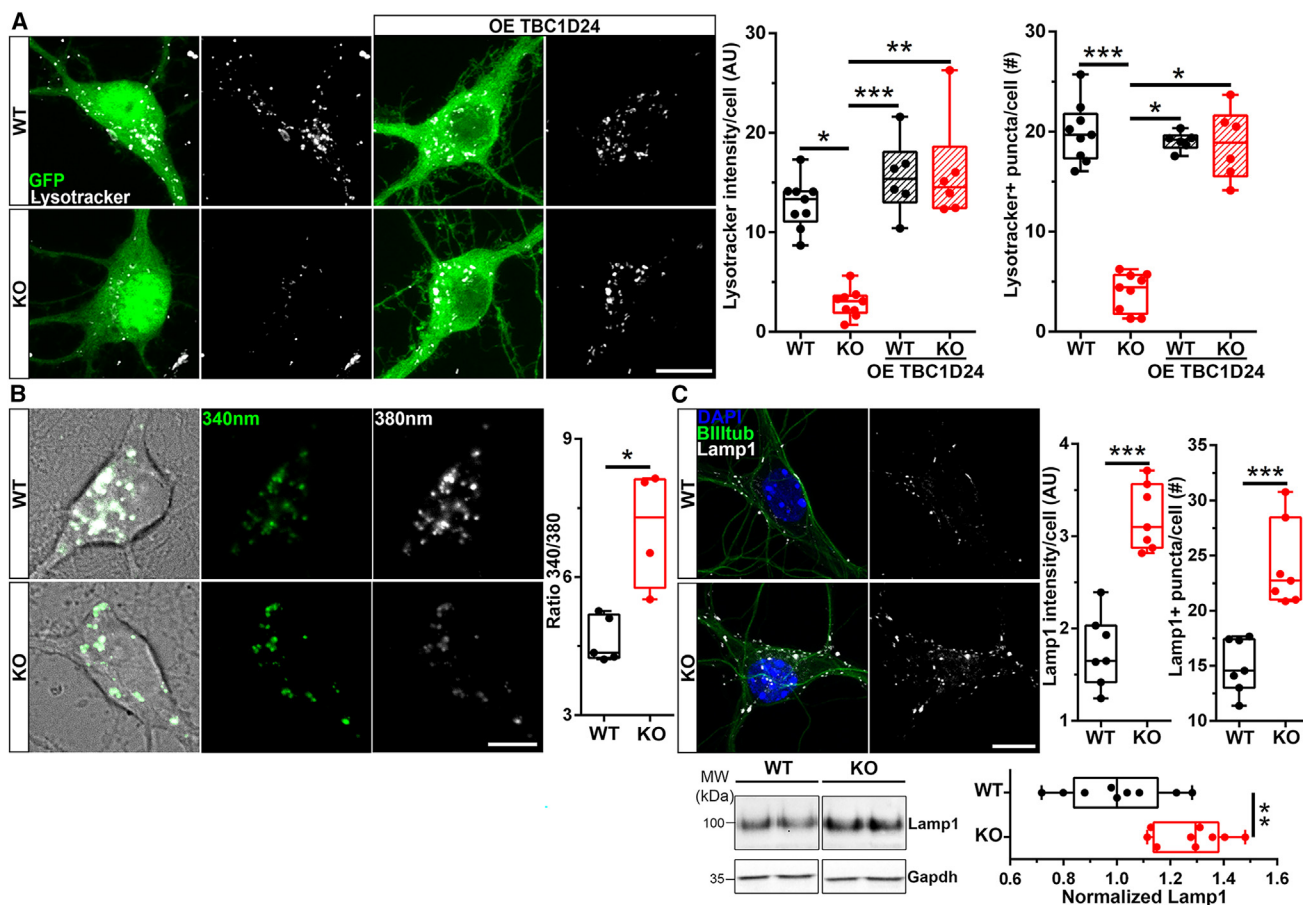


Figure 5. Tbc1d24 KO neurons present increased pH at intracellular organelles

(A) *Left*: Representative images of LysoTracker and GFP signals in WT and KO hippocampal neurons transfected with either pCAGG-GFP empty vector or TBC1D24-pCAGG-GFP (OE TBC1D24) (12 DIV). *Right*: LysoTracker mean fluorescent intensity and positive puncta quantifications at neuronal soma, identified by GFP signal. Boxplots (center line, median [Q2]; box limits, 25th [Q1]-75th [Q3] percentiles; whisker length, the outermost data points within 3-fold the interquartile range [Q3-Q1]) of 9 replications for WT and KO and 6 replications for OE. Each dot represents the mean fluorescent intensity of 20–47 neurons prepared from a single embryo. * $p < 0.05$, ** $p < 0.01$, *** $p < 0.001$, Kruskal-Wallis/Dunn's test.

(B) *Left*: Representative images of LysoSensor yellow/blue DND-160 live staining at 340 nm (green) and 380 nm (red) excitation in WT and KO hippocampal neurons (12 DIV). Merged 340/380 and brightfield images are also shown. *Right*: LysoSensor yellow/blue DND-160 ratio (340/380 nm) at neuronal soma, identified in bright field. Boxplots (center line, median [Q2]; box limits, 25th [Q1]-75th [Q3] percentiles; whisker length, the outermost data points within 3-fold the interquartile range [Q3-Q1]) of 5 (WT) or 4 (KO) replications. Each dot represents the mean ratio of 15–30 neurons prepared from a single embryo. * $p < 0.05$, Mann-Whitney U-test.

(C) *Upper left*: Representative images of Lamp1, β -III tubulin and DAPI staining in WT and KO hippocampal neurons (12 DIV). *Upper right*: Lamp1 signal at neuronal soma, identified by β -III tubulin staining. Boxplots (center line, median [Q2]; box limits, 25th [Q1]-75th [Q3] percentiles; whisker length, the outermost data points within 3-fold the interquartile range [Q3-Q1]) of 7 replications. Each dot represents the mean of 15–30 neurons prepared from a single embryo. *** $p < 0.001$, Mann-Whitney U-test. *Lower left*: Representative Western blotting of Lamp1 from WT and KO cortical neurons (12 DIV). *Lower right*: Densitometric analysis of Lamp1 signal normalized on Gapdh and expressed as percentage of WT. Boxplots (center line, median [Q2]; box limits, 25th [Q1]-75th [Q3] percentiles; whisker length, the outermost data points within 3-fold the interquartile range [Q3-Q1]) of 9 replications. Each dot represents neuronal lysate from a single embryo. ** $p < 0.01$, unpaired Student's *t* test. Scale bars, 10 μ m.

probes and normalize the signal for each analyzed bouton (Fmax) (Figure 8A). The measured F0, FQ before and after stimulation and Fmax values were employed to evaluate SypHy surface fraction and average pH of SVs, following a previously reported method with minor modifications³¹ (Figure S5B). In the basal condition, no significant differences in fluorescent values, or the pH of SVs were detected by comparing WT and KO synapses, suggesting that under resting condition KO synapses

do not display a major defect in SV pH homeostasis (Figures 8B and S5B). The basal surface fraction was slightly increased, suggesting a defective SV cycling at KO synapses (Figure 8A). When SV release and recycling was induced by KCl stimulation, the fluorescence increase was comparable between the two genotypes, but the recovery of the fluorescence after the stimulation was significantly impaired (Figure 8A). This indicates defective endocytosis and/or reacidification. When

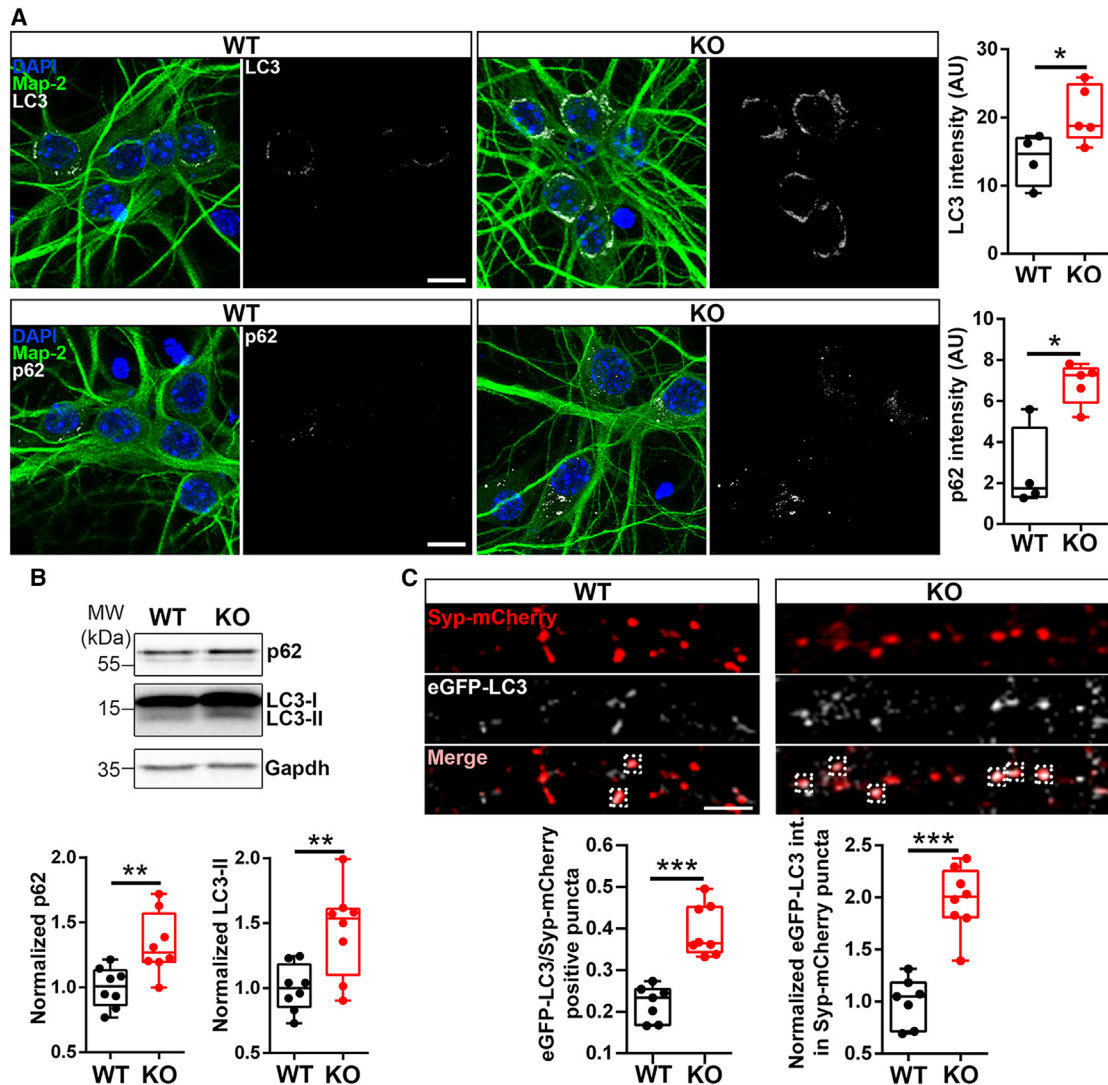


Figure 6. Tbc1d24 KO neurons show impaired autophagy

(A) *Right*: Representative images of DAPI signal and Map-2, LC3 (*top*) and p62 (*bottom*) immunostaining in WT and KO hippocampal neurons (12 DIV). Scale bar, 10 μ m. *Left*: LC3 (*top*) and p62 (*bottom*) fluorescence intensity evaluated at somatic level identified by Map-2 signal. Boxplots (center line, median [Q2]; box limits, 25th [Q1]-75th [Q3] percentiles; whisker length, the outermost data points within 3-fold the interquartile range [Q3-Q1]) of 4 (WT) or 5 (KO) replications. Each dot represents the mean fluorescent intensity of 20–43 neurons prepared from a single embryo. * $p < 0.05$, Mann-Whitney U-test.

(B) *Top*: Representative Western blotting of p62 and LC3-I/II, from WT and KO cortical neurons (12 DIV); Gapdh is shown as loading control. *Bottom*: Boxplots (center line, median [Q2]; box limits, 25th [Q1]-75th [Q3] percentiles; whisker length, the outermost data points within 3-fold the interquartile range [Q3-Q1]) of LC3-II and p62 densitometric analysis normalized on Gapdh signal. KO values are expressed as percentage of WT. Each dot represents neuronal lysate from a single embryo ($n = 8$). ** $p < 0.01$, unpaired Student's t test.

(C) *Top*: Representative images of Syp-mCherry and eGFP-LC3 in WT and KO hippocampal neurons (18 DIV) transduced with FU-Syp-mCherry-P2A-eGFP-LC3 lentiviral vector at 14 DIV. Dotted squares show colocalization puncta. Scale bar, 5 μ m. *Bottom*: Percentage of eGFP-LC3/Syp-mCherry double-positive puncta with respect to Syp-mCherry positive puncta and normalized mean fluorescence intensity of eGFP-LC3 in Syp-mCherry positive puncta expressed in percent of the WT. 25 branches and 50 Syp-mCherry positive puncta from five different fields were analyzed for each coverslip. Boxplots (center line, median [Q2]; box limits, 25th [Q1]-75th [Q3] percentiles; whisker length, the outermost data points within 3-fold the interquartile range [Q3-Q1]) of 7 (WT) or 8 (KO) replications. Each dot represents the mean value for one coverslip from 4 to 5 neuronal preparations. *** $p < 0.001$, unpaired Student's t test/Mann-Whitney U-test.

measured after the stimulation, the pH of SVs and the surface fraction were increased in KO synapses in respect to WT, suggesting that both processes of post stimulus endocytosis and reacidification were impaired. This is confirmed by comparing the differences in pH and surface fraction before and after stimula-

tion (Figures 8B and 8C). Interestingly, when the differences of the two parameters before and after stimulation were calculated for the two genotypes at same synaptic boutons, endocytosed SV were properly acidified in WT but more basic in KO synapses (Figures 8B and 8C). Taken together, these data suggest that

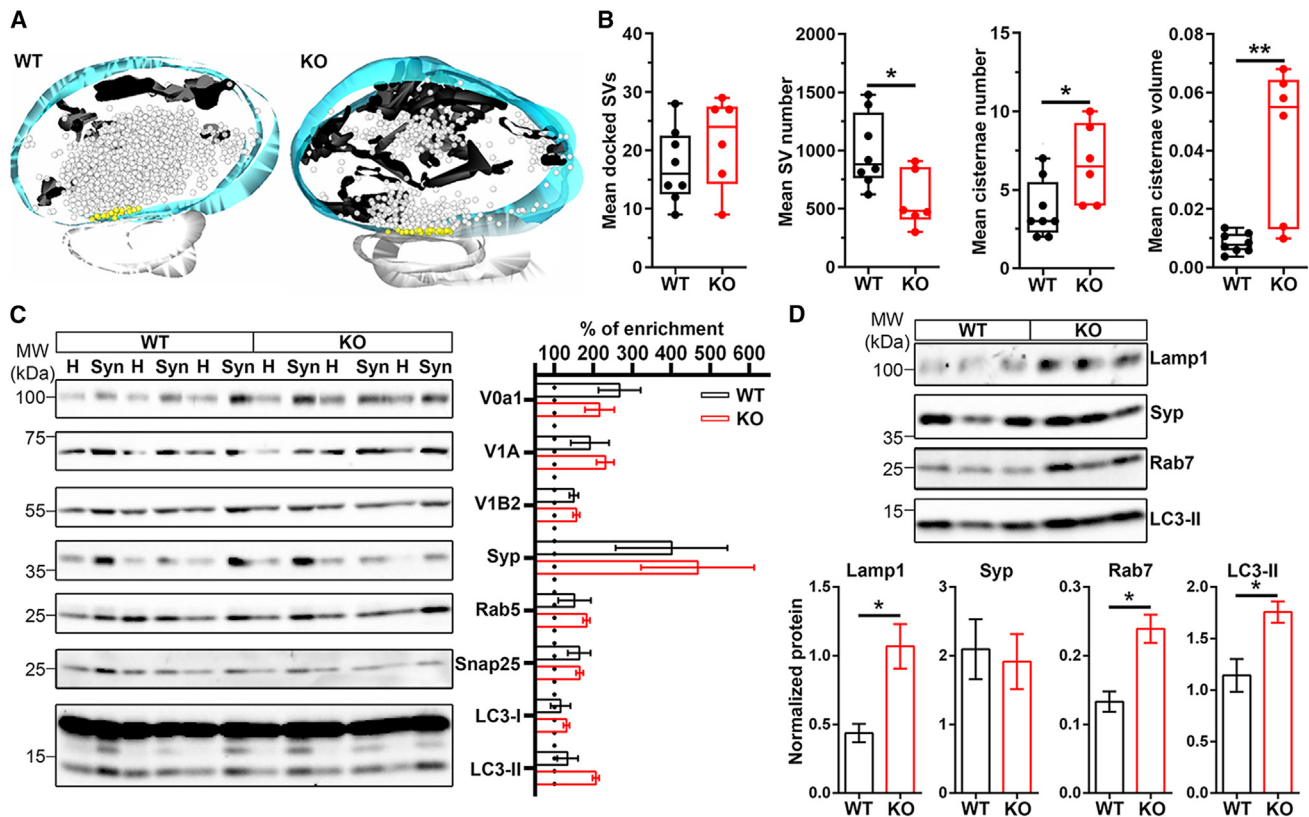


Figure 7. Tbc1d24 loss modifies nerve terminal ultrastructure and results in Lamp1, Rab7 and LC3-II synaptic accumulation

(A) Three-dimensional reconstructions of synaptic terminals from serial ultrathin sections; shown are representative three-dimensional reconstructions from 60 nm-thick serial sections obtained WT and KO synapses. Total SVs and SVs physically docked at the AZ are depicted as blue and yellow spheres, respectively. The AZ and cisternal structures are shown in yellow and black, respectively.

(B) Morphometric analysis. Boxplots (center line, median [Q2]; box limits, 25th [Q1]-75th [Q3] percentiles; whisker length, the outermost data points within 3-fold the interquartile range [Q3-Q1]) of 8 (WT) or 6 (KO) replications. The analysis of three-dimensionally reconstructed synapses displayed reduced total SVs and increased endosomal number and volume. * $p < 0.05$, ** $p < 0.01$, Mann-Whitney U-test.

(C) Left: Western Blotting of Atp6V0a1 (V0a1), Atp6v1a (V1A), Atp6v1b2 (V1B2), Synaptophysin-1 (Syp), Rab5, Snap-25 and LC3-I/II from total lysate (H) and synaptosomal fractions (Syn) of WT and KO cortical neurons (14 DIV). Right: Quantification of indicated proteins' enrichment in synaptosomal fractions of WT and KO neurons. Protein signals were normalized on Ponceau-S and expressed as percentage of the respective homogenate. Data are represented as mean \pm SEM of $n = 3$ neuronal preparations.

(D) Top: Western Blotting of Lamp1, Syp, Rab7 and LC3-II from synaptosomal fractions as in C. Bottom: Bar plots of the densitometric analysis normalized on Ponceau-S. Data are represented as mean \pm SEM of $n = 3$ neuronal preparations. * $p < 0.05$, unpaired Student's t test.

Tbc1d24 facilitates SV reacidification and proper recycling and clearance of intra-terminal cisternae at synaptic boutons.

DISCUSSION

The v-ATPase is a multi-subunit proton pump essential for neuronal function. Its activity must be controlled exquisitely in the brain; not only to maintain the necessary physiological pH gradient across the endo-lysosomal system for autophagic processes, but also to generate the electrochemical gradient required for neurotransmitter loading into SVs.^{32,33} Several mutations in genes coding for v-ATPase subunits have been described recently in patients with neurodevelopmental disorders that include intellectual disabilities and seizures, highlighting the significance of this complex for brain physiology.^{4–6,8,34–36} However, little is known regarding the modality

of v-ATPase function in the brain and the specific neuronal interactors and regulators.

The interaction between v-ATPase complex and the TLDC domain protein family, including NCOA7, OXR1, TBC1D24, TLDC1/mEAK7 and TLDC2, has been described recently *in vitro*.¹⁸ However, somewhat contradictory results have emerged from biochemical, structural, and cellular studies describing the potential functional significance of these interactions to date.³⁷ In particular, structural studies of yeast OXR1p revealed that the protein, together with the recently characterized yeast TLDC protein RC5, disassembles the V₁ and V₀ subunits thus exerting an inhibitory action on the pump.^{38–40} Adding further complexity to the functional relationship, yeast OXR1p also regulates subcellular compartmentalization of v-ATPase subunits.³⁹ However, cryo-EM analysis of the TLDC1/mEAK7:v-ATPase interaction demonstrated a subtly different

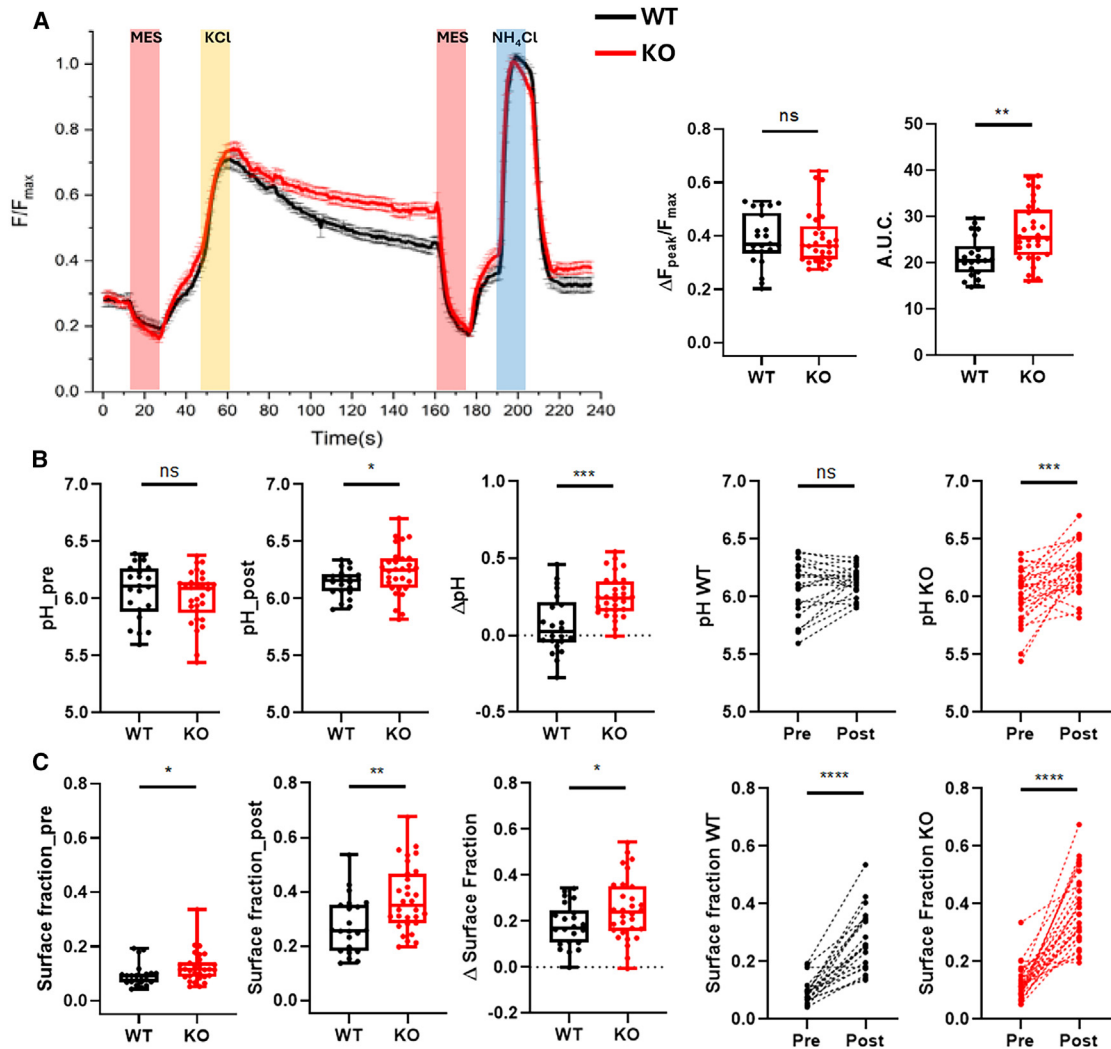


Figure 8. Tbc1d24 KO neurons show impaired SV endocytosis and reacidification

(A) *Left*: Average traces of SpHy fluorescence plotted for WT (black trace) and KO (red trace) neurons in response to acidic quenching (pink; MES, pH 5.5) before and after KCl stimulation (yellow; KCl, 50 mM) and followed by ammonium solution (light blue; NH_4Cl 50 mM, pH 7.4); 20–50 ROIs are analyzed for each coverslip. Data (F/F_{max}) are shown as mean \pm SEM from 22 (WT) and 30 (KO) coverslips from 5 independent neuronal preparations. *Right*: Peak fluorescence upon KCl stimulation ($\Delta F_{\text{peak}}/F_{\text{max}}$) and area under the curve after KCl stimulation (AUC) to evaluate SV exocytosis and endocytosis/reacidification. Boxplots (center line, median [Q2]; box limits, 25th [Q1]–75th [Q3] percentiles; whisker length, the outermost data points within 3-fold the interquartile range [Q3–Q1]) of 22 (WT) or 30 (KO) replications. Each dot represents the mean value for one coverslip from 4 neuronal preparations. ** $p < 0.01$, Mann-Whitney U-test.

(B) *Left*, Boxplots (center line, median [Q2]; box limits, 25th [Q1]–75th [Q3] percentiles; whisker length, the outermost data points within 3-fold the interquartile range [Q3–Q1]) of SV pH before (pH_{pre}) and after (pH_{post}) stimulation and their difference ($\Delta\text{pH} = [\text{pH}_{\text{post}} - \text{pH}_{\text{pre}}]$) calculated from the above experiments. * $p < 0.05$, *** $p < 0.001$ unpaired Student's *t* test. *Right*, pH values before and after stimulation for WT and KO synapses. *** $p < 0.001$, paired Student's *t* test.

(C) *Left*, Boxplots (center line, median [Q2]; box limits, 25th [Q1]–75th [Q3] percentiles; whisker length, the outermost data points within 3-fold the interquartile range [Q3–Q1]) of surface fraction before (Surface fraction_{pre}) and after (Surface fraction_{post}) stimulation and their difference ($\Delta\text{Surface fraction} = [\text{Surface fraction}_{\text{post}} - \text{Surface fraction}_{\text{pre}}]$) calculated from the above experiments. * $p < 0.05$, ** $p < 0.01$ unpaired Student's *t* test. *Right*, Surface fraction values before and after stimulation for WT and KO synapses. **** $p < 0.0001$, paired Student's *t* test. Each dot represents the mean value for one coverslip.

interaction that does not appear to alter v-ATPase activity.^{41,42}

More recently *in vitro* reconstitution of the v-ATPase/TLDC protein complex suggest that TLDC2, NCOA7, OXR1, and TBC1D24 appear to inhibit v-ATPase by inducing enzyme disassembly, whereas mEAK7 activates the pump.⁴³ In contrast, an increase in lysosomal pH in neurons alongside a reduction in membrane-associated V_1 subunits were revealed upon deletion

of the *Ncoa7* gene in mice,⁴⁴ suggesting a supportive effect of NCOA7 on V-ATPase assembly and activity. Thus, it is apparent that the cellular, tissue and context-specific actions of different TLDC proteins influence v-ATPase functionality.

In the present study, we reveal that TBC1D24 interacts with the V_1 subunits of v-ATPase in the mammalian brain, and in its absence, the V_1/V_0 association is impaired in neuronal cells.

This, in turn, results in defective acidification of the endo-lysosomal compartments and SVs, alongside autophagic impairment at neuronal soma and synaptic terminals. Furthermore, the V₁ subunit ATP6V1B2 and TBC1D24 show a high level of colocalization in neurons and along neuronal branches. We propose that TBC1D24 is an important regulator of v-ATPase assembly and activity in neurons; the functional interaction supports neuronal autophagy while also acting at presynaptic sites, where it regulates SV reacidification and the maintenance of the reserve pool of SVs.

TBC1D24, NCOA7 and OXR1 mRNAs are highly expressed in central nervous system,⁴² especially in the cerebral cortex, hippocampus and cerebellum where they may exert opposing and/or ancillary regulatory roles to modulate v-ATPase function. In addition, differential cell-type expression of TBC1D24 and NCOA7 suggest that TLDC proteins can also play specific roles in neuronal subtypes.⁴⁵ Structurally, NCOA7 and TBC1D24 contain a PIP binding domain which may facilitate the association of the C-terminal TLDC domain with V₁ subunits. Here, we observed a highly similar PIP binding profile for TBC1D24 when compared to NCOA7, including PI(3)P and PI(5)P that are enriched in early endosomes and autophagosomes, along with PI(3,5)P2 and PI(4,5)P2, enriched in the late endosomes and lysosomes.⁴⁶ These data support a role for the two TLDC proteins in the active acidification of endo-lysosomal organelles in neurons. Furthermore, binding of the TBC1D24 *Drosophila* orthologue skywalker protein to specific PIPs has been studied in detail, highlighting how conserved disease-causing mutations influence PIP association.¹⁶

With respect to NCOA7 and the other TLDC proteins, TBC1D24 contains the unique combination of the C-terminal TLDC domain with the TBC domain at the N-terminus. Interestingly, Eaton et al.¹⁸ demonstrated that the full-length TBC1D24 protein is necessary for the interaction with the v-ATPase to occur *in vitro*, suggesting some allosteric/cooperative role of the amino-terminal TBC domain. Moreover, the TBC domain of TBC1D24 interacts with Arf6 and regulates the activation state of the small GTPase^{20,24,47} (and this paper). The interplay between these two proteins is demonstrated by the similar presynaptic ultrastructure in neurons when Arf6 expression is knocked down.⁴⁸ Of note, Arf6 is a regulator of the v-ATPase assembly state,²³ corroborating the functional interplay between Tbc1d24, Arf6 and v-ATPase in neurons.

Whether these structural N-terminal relationships are a key feature of v-ATPase regulation by TLDC proteins warrants further investigation, particularly given the important role of defined PIP lipid enrichment on the membranes of intracellular structures that might provide organelle-specific functional regulation by TLDC proteins.²² It is clear that the TLDC domain is an evolutionary-conserved v-ATPase modulatory factor with potentially diverse mechanisms. Indeed, the short, interferon-induced TLDC domain isoform of NCOA7 (NCOA7B) has been shown to mediate viral infection by altering endosomal pH homeostasis via v-ATPase⁴⁹; therefore, there is still much to learn regarding the context-specific actions of TLDC proteins in and around v-ATPase functionality.

Among the diverse TLDC proteins, TBC1D24 is particularly relevant in neurons for the reported enrichment at synaptic

sites²⁸ and the synaptic phenotype of *Tbc1d24* loss-of-function models both in *Drosophila* and mammals.^{15,20,21} Here, we confirm synaptic enrichment of Tbc1d24 in the cerebral cortex and expression at presynaptic and postsynaptic sites. Based on our live imaging data, we suggest that TBC1D24 acts as a chaperone assisting the correct assembly of the v-ATPase proton pump during SV recycling. Recently, the cryo-EM structure of a mammalian v-ATPase in native synaptic vesicle revealed dissociation of V1 complex upon neurotransmitter loading, to mark SVs that are ready for exocytosis.⁵⁰ This implies the need of correct v-ATPase reassembly upon SV endocytosis to allow SV reacidification and recycling.

Previous work has supported the role of TBC1D24 in SV cycling and neurotransmission,^{15,21} although the molecular mechanisms, particularly at the level of mammalian central synapses, are largely unknown. In *Drosophila*, skywalker has been shown to regulate SV protein degradation via the interaction with the small GTPase Rab35 and, in larval neuromuscular junctions (NMJs), sky mutants display an increased readily releasable pool of SVs and altered protein turnover due to uncontrolled degradation.^{21,51} In murine neurons, both haploinsufficiency¹⁵ and total loss of *Tbc1d24*, as revealed in this paper, result in the accumulation of endosomal-like structures at synaptic terminals, as reported at the *Drosophila* larvae NMJs. However, in mammalian cells, Tbc1d24 was demonstrated to interact with the small GTPase Arf6 rather than Rab35²⁰ and the evidence of an enlarged readily releasable pool of SVs at presynaptic sites is not recapitulated¹⁵ (and this paper). Based on the live imaging and biochemical data, we suggest that these cisternae-like structures represent intermediates in the SV cycling that result from defective stimulus-induced recycling and reacidification. In addition, this aberrant presynaptic phenotype is associated with accumulation of endolysosomal and autophagy markers at synaptic sites and with a net decrease in the total SV number, suggesting defective SV reformation and increased degradative load at the synapse. In accordance, presynaptic protein degradation is reported to rely on autophagy³⁰ and/or lysosomal degradation, with presynaptic lysosome-related vesicles transported to axon terminals and involved in presynaptic biogenesis and maintenance.^{52,53}

Similarly, the mammalian homologue of the Rav1 member for the RAVE complex, DMXL2, has been proposed to regulate SV acidification^{32,54}; furthermore, recessive *DMXL2* mutations have been described in patients with epileptic encephalopathy that cause pH dysregulation and autophagy impairment.⁵⁵ This points to multiple regulatory factors that are required for the regulation of the SV pH at synapses, which can depend on synaptic subtypes, activation state, and plasticity. In this context, it has to be considered that SVs in GABAergic and glutamatergic synapses have been shown to display different pH values,³¹ predominantly, but not entirely, attributable to the respective expression of the neurotransmitter transporter types. This, in turn, impacts on the kinetics of neurotransmitter loading and the probability of release.^{56,57} *TBC1D24* mRNA is preferentially expressed in cortical, hippocampal, and cerebellar excitatory neurons, suggesting that it primarily acts at glutamatergic synapses.^{43,45} Here, we describe the functional effects of *Tbc1d24* loss at hippocampal synapses in primary cultures, which are mostly excitatory glutamatergic synapses. Future work is

needed to unravel the role of TBC1D24 at other synaptic subtypes and study additional synaptic v-ATPase regulators that act in a similar fashion.

TBC1D24 is a pleiotropic gene mutated in a spectrum of neurodevelopmental disorders. The numerous pathogenic mutations described are typically homozygous or compound heterozygous with epileptic encephalopathy and neurodegeneration as the more severe clinical manifestations. It has been suggested that homozygous *TBC1D24* loss-of-function correlates with the most severe prognosis, although the broad clinical spectrum and the range of variants do not define a clear genotype-phenotype association.¹⁴ Although relatively few studies have investigated human TBC1D24 protein levels in the context of disease, evidence for an almost complete loss of expression have been provided for patients with DOORS syndrome or lethal familial neonatal seizures.^{12,58} In addition, TBC1D24 patients affected by the most severe epileptic phenotypes and neurodegenerative manifestations bear frameshift mutations, predicted to result in residual or absent expression of the TBC1D24 protein.⁵⁹ Loss of protein stability has been also proposed for missense mutations that cause focal epilepsy or progressive myoclonic epilepsy.^{20,60,61} Here, we model the complete loss of mammalian *Tbc1d24* *in vivo* and propose that dysregulation of pH homeostasis and autophagy in neurons and synapses are at the basis of the TBC1D24 loss-of-function phenotype. These data are supported by the clinical observation of analogous phenotypes in patients bearing *TBC1D24* mutations or pathogenic variants in the gene coding for the V_1 subunit *ATP6V1B2*. Mutations in the two genes are causative for 45% of the known cases of the rare DOORS syndromes⁹ and *de novo* *ATP6V1B2* mutations result in a loss-of-function phenotype with impairment of lysosomal acidification.⁶² In addition, the two genes are mutated in a spectrum of epileptic encephalopathies characterized by early infantile manifestation, intellectual disability and seizures.^{10,14} The involvement of either *TBC1D24* or *ATP6V1B2* mutations in these very specific, phenotypically overlapping syndromes strongly support a pivotal role of the loss of pH homeostasis and SV reacidification in the disease pathogenesis. Further studies are needed to define the extent of lysosomal and autophagic impairment in TBC1D24 loss of function models and its role in neuronal and synaptic function. The data presented here suggest the reestablishment of pH homeostasis as a possible therapeutic strategy for this class of disorders.

Limitations of the study

Although our study reveals that TBC1D24 is a regulator of v-ATPase assembly and function in live neurons, as well as playing a role in synaptic vesicle reacidification at presynaptic terminals, there are still questions that need to be addressed. For example, TBC1D24 is expressed in non-neuronal cells in addition to being enriched at neuronal postsynaptic sites; therefore, we could ask about the potential contribution of TBC1D24 on v-ATPase function outside the brain and in the regulation of postsynaptic receptors. In this study, we demonstrated the important contribution of TBC1D24 for synaptic vesicle recycling and reacidification; however, further studies of the impact of TBC1D24 loss on neurotransmission are required. Finally, the role of TBC1D24 in the regulation of v-ATPase is of significance for the disease's mech-

anisms, such that pathophysiological studies will help to understand the relevance of our study to specific neurodevelopmental disorders caused by v-ATPase and TBC1D24 variants. Pathophysiological studies are needed, given the growing number of pathogenic variants described, likely representing more complex functional alleles than complete loss-of-function.

RESOURCE AVAILABILITY

Lead contact

Further information and requests for resources and reagents should be directed to and will be fulfilled by the lead contact Anna Fassio (anna.fassio@unige.it).

Material availability

The *Tbc1d24*^{INS2/INS2} mouse (KO) line generated in this study is deposited at The Mary Lyon Centre, UK; the internal reference code is TBC1D24-INS2-EM4-B6. The antibody generated in this study is available upon request, however there are restrictions as to the availability due to the limited amount generated. Other commercial antibodies can substitute our custom antibody such as Novus NBP1-82925, alternatively used in this paper.

Data and code availability

- Data: All data reported in this paper will be shared by the [lead contact](#) upon request.
- Code: This paper does not report original code.
- Other items: Any additional information required to reanalyze the data reported in this paper is available from the [lead contact](#) upon request.

ACKNOWLEDGMENTS

We thank the transgenic core and molecular biology teams at the MRC Harwell Institute Mary Lyon Center for the design, generation and quality control of the *Tbc1d24* null model, in particular Gemma Codner and Lydia Teboul. We are also very grateful for assistance from the animal care staff at The Mary Lyon Center, in particular Ward 6 staff including Simona Oliveri, Eddie Chambers, and Simon Gillard. We thank Caterina Valetti, University of Genoa, for helpful discussion and assistance with the morphometric analysis and Erica Tagliatti, Humanitas University, for support in vector cloning. This work was supported by #NEXTGENERATIONEU National Recovery and Resilience Plan (NRRP), project MNESYS PE0000006 – A Multiscale integrated approach to the study of the nervous system in health and disease DN. 1553 11.10.2022 and by a research grant from the University of Pennsylvania Orphan Disease Center in partnership with the TBC1D24 Foundation to AF, in addition to a Medical Research Council Programme Grant (MR/P502005/1) and Epilepsy Research UK pilot grant (P1805) to PLO.

AUTHOR CONTRIBUTIONS

S.P. and D.A. performed primary culture preparation, live imaging, immunocytochemistry, biochemical experiments, data analysis, and figure preparation. S.G. performed live imaging experiments. E.C. performed EM acquisition and analysis. A.M. contributed to biochemical experiments and primary culture preparation. S.H. contributed to animal model generation and handling. A.P. and T.S. contributed to mouse model characterization and pull-down experiments. F.B. contributed to data interpretation and paper preparation. P.O. and A.F. planned the experiments, interpreted the data, wrote the paper and funded the research. All of the authors contributed to the final version of the manuscript.

DECLARATION OF INTERESTS

The authors declare no competing interests.

STAR★METHODS

Detailed methods are provided in the online version of this paper and include the following:

- **KEY RESOURCES TABLE**
- **EXPERIMENTAL MODEL AND STUDY PARTICIPANT DETAILS**
 - Tbc1d24 null mouse model
 - Ethical statement for animal experiments
 - Mouse and rat primary cultures
 - COS-7 cell culture
 - Custom antibody production
- **METHOD DETAILS**
 - Embryo histology and *in situ* hybridisation
 - Constructs
 - Cell transfection
 - Cell transduction
 - Pull-down
 - Immunoprecipitation from brain tissue
 - Cytosol/membrane fractionation
 - Synaptosomes from rat brain and primary neurons
 - Arf6 activation state evaluation
 - Western blotting
 - Electron microscopy
 - LysoTracker and Lysosensor experiments
 - Immunocytochemistry
 - Live-imaging pfluorin experiments
 - Calibration of pfluorin probe
- **QUANTIFICATION AND STATISTICAL ANALYSIS**
 - Imaging analysis
 - Statistical analysis

SUPPLEMENTAL INFORMATION

Supplemental information can be found online at <https://doi.org/10.1016/j.isci.2024.111515>.

Received: December 12, 2023

Revised: September 29, 2024

Accepted: November 28, 2024

Published: December 1, 2024

REFERENCES

1. Abbas, Y.M., Wu, D., Bueler, S.A., Robinson, C.V., and Rubinstein, J.L. (2020). Structure of V-ATPase from the mammalian brain. *Science* 367, 1240–1246. <https://doi.org/10.1126/science.aaz2924>.
2. Bodzeta, A., Kahms, M., and Klingauf, J. (2017). The Presynaptic v-ATPase Reversibly Disassembles and Thereby Modulates Exocytosis but Is Not Part of the Fusion Machinery. *Cell Rep.* 20, 1348–1359. <https://doi.org/10.1016/j.celrep.2017.07.040>.
3. Farsi, Z., Gowrisankaran, S., Krunic, M., Rammner, B., Woehler, A., Lafer, E.M., Mim, C., Jahn, R., and Milosevic, I. (2018). Clathrin coat controls synaptic vesicle acidification by blocking vacuolar ATPase activity. *Elife* 7, e32569. <https://doi.org/10.7554/eLife.32569>.
4. Guerrini, R., Mei, D., Kerti-Szigeti, K., Pepe, S., Koenig, M.K., Von Allmen, G., Cho, M.T., McDonald, K., Baker, J., Bhambhani, V., et al. (2022). Phenotypic and genetic spectrum of ATP6V1A encephalopathy: a disorder of lysosomal homeostasis. *Brain* 145, 2687–2703. <https://doi.org/10.1093/brain/awac145>.
5. Mattison, K.A., Tossing, G., Mulroe, F., Simmons, C., Butler, K.M., Schreiber, A., Alsadah, A., Neilson, D.E., Naess, K., Wedell, A., et al. (2023). ATP6V0C variants impair V-ATPase function causing a neurodevelopmental disorder often associated with epilepsy. *Brain* 146, 1357–1372. <https://doi.org/10.1093/brain/awac330>.
6. Indrawinata, K., Argiropoulos, P., and Sugita, S. (2023). Structural and functional understanding of disease-associated mutations in V-ATPase subunit a1 and other isoforms. *Front. Mol. Neurosci.* 16, 1135015. <https://doi.org/10.3389/fnmol.2023.1135015>.
7. Gupta, H.V., Vengoechea, J., Sahaya, K., and Virmani, T. (2015). A splice site mutation in ATP6AP2 causes X-linked intellectual disability, epilepsy, and parkinsonism. *Parkinsonism Relat. Disorders* 21, 1473–1475. <https://doi.org/10.1016/j.parkreldis.2015.10.001>.
8. Fassio, A., Esposito, A., Kato, M., Saitsu, H., Mei, D., Marini, C., Conti, V., Nakashima, M., Okamoto, N., Olmez Turker, A., et al. (2018). De novo mutations of the ATP6V1A gene cause developmental encephalopathy with epilepsy. *Brain* 141, 1703–1718. <https://doi.org/10.1093/brain/awy092>.
9. Beauregard-Lacroix, E., Pacheco-Cuellar, G., Ajeawung, N.F., Tardif, J., Dieterich, K., Dabir, T., Vind-Kezunovic, D., White, S.M., Zadori, D., Castiglioni, C., et al. (2021). DOORS syndrome and a recurrent truncating ATP6V1B2 variant. *Genet. Med.* 23, 149–154. <https://doi.org/10.1038/s41436-020-00950-9>.
10. Veltra, D., Kosma, K., Papavasiliou, A., Tilemis, F.N., Traeger-Synodinos, J., and Sofocleous, C. (2022). A novel pathogenic ATP6V1B2 variant: Widening the genotypic spectrum of the epileptic neurodevelopmental phenotype. *Am. J. Med. Genet.* 188, 3563–3566. <https://doi.org/10.1002/ajmg.a.62971>.
11. Qiu, S., Zhao, W., Gao, X., Li, D., Wang, W., Gao, B., Han, W., Yang, S., Dai, P., Cao, P., and Yuan, Y. (2021). Syndromic Deafness Gene ATP6V1B2 Controls Degeneration of Spiral Ganglion Neurons Through Modulating Proton Flux. *Front. Cell Dev. Biol.* 9, 742714. <https://doi.org/10.3389/fcell.2021.742714>.
12. Campeau, P.M., Kasperaviciute, D., Lu, J.T., Burrage, L.C., Kim, C., Hori, M., Powell, B.R., Stewart, F., Félix, T.M., van den Ende, J., et al. (2014). The genetic basis of DOORS syndrome: an exome-sequencing study. *Lancet Neurol.* 13, 44–58. [https://doi.org/10.1016/S1474-4422\(13\)70265-5](https://doi.org/10.1016/S1474-4422(13)70265-5).
13. Mucha, B.E., Hennekam, R.C.M., Sisodiya, S., and Campeau, P.M. (1993). TBC1D24-Related Disorders. In *Prereviews(R)*, M.P. Adam, D.B. Everman, G.M. Mirzaa, R.A. Pagon, S.E. Wallace, L.J.H. Bean, K.W. Gripp, and A. Amemiya, eds.
14. Balestrini, S., Milh, M., Castiglioni, C., Lüthy, K., Finelli, M.J., Verstreken, P., Cardon, A., Stražisar, B.G., Holder, J.L., Jr., Lesca, G., et al. (2016). TBC1D24 genotype-phenotype correlation: Epilepsies and other neurologic features. *Neurology* 87, 77–85. <https://doi.org/10.1212/WNL.0000000000002807>.
15. Finelli, M.J., Aprile, D., Castroflorio, E., Jeans, A., Moschetta, M., Chesum, L., Degiacomi, M.T., Grasegger, J., Lupien-Meilleur, A., Bassett, A., et al. (2019). The epilepsy-associated protein TBC1D24 is required for normal development, survival and vesicle trafficking in mammalian neurons. *Hum. Mol. Genet.* 28, 584–597. <https://doi.org/10.1093/hmg/ddy370>.
16. Fischer, B., Lüthy, K., Paesmans, J., De Koninck, C., Maes, I., Swerts, J., Kuenen, S., Uytterhoeven, V., Verstreken, P., and Versées, W. (2016). Sky-walker-TBC1D24 has a lipid-binding pocket mutated in epilepsy and required for synaptic function. *Nat. Struct. Mol. Biol.* 23, 965–973. <https://doi.org/10.1038/nsmb.3297>.
17. Wang, J., Rousseau, J., Kim, E., Ehresmann, S., Cheng, Y.T., Duraine, L., Zuo, Z., Park, Y.J., Li-Kroeger, D., Bi, W., et al. (2019). Loss of Oxidation Resistance 1, OXR1, Is Associated with an Autosomal-Recessive Neurological Disease with Cerebellar Atrophy and Lysosomal Dysfunction. *Am. J. Hum. Genet.* 105, 1237–1253. <https://doi.org/10.1016/j.ajhg.2019.11.002>.
18. Eaton, A.F., Brown, D., and Merkulova, M. (2021). The evolutionary conserved TLDc domain defines a new class of (H(+))V-ATPase interacting proteins. *Sci. Rep.* 11, 22654. <https://doi.org/10.1038/s41598-021-01809-y>.
19. Cotter, K., Stransky, L., McGuire, C., and Forgac, M. (2015). Recent Insights into the Structure, Regulation, and Function of the V-ATPases.

- Trends Biochem. Sci. 40, 611–622. <https://doi.org/10.1016/j.tibs.2015.08.005>.
20. Lin, L., Lyu, Q., Kwan, P.Y., Zhao, J., Fan, R., Chai, A., Lai, C.S.W., Chan, Y.S., Shen, X., and Lai, K.O. (2020). The epilepsy and intellectual disability-associated protein TBC1D24 regulates the maintenance of excitatory synapses and animal behaviors. *PLoS Genet.* 16, e1008587. <https://doi.org/10.1371/journal.pgen.1008587>.
 21. Uytterhoeven, V., Kuenen, S., Kasprovicz, J., Miskiewicz, K., and Verstreken, P. (2011). Loss of skywalker reveals synaptic endosomes as sorting stations for synaptic vesicle proteins. *Cell* 145, 117–132. <https://doi.org/10.1016/j.cell.2011.02.039>.
 22. Banerjee, S., and Kane, P.M. (2020). Regulation of V-ATPase Activity and Organelle pH by Phosphatidylinositol Phosphate Lipids. *Front. Cell Dev. Biol.* 8, 510. <https://doi.org/10.3389/fcell.2020.00510>.
 23. Hurtado-Lorenzo, A., Skinner, M., El Annan, J., Futai, M., Sun-Wada, G.H., Bourgoin, S., Casanova, J., Wildeman, A., Bechoua, S., Ausiello, D.A., et al. (2006). V-ATPase interacts with ARNO and Arf6 in early endosomes and regulates the protein degradative pathway. *Nat. Cell Biol.* 8, 124–136. <https://doi.org/10.1038/ncb1348>.
 24. Aprile, D., Fruscione, F., Baldassari, S., Fadda, M., Ferrante, D., Falace, A., Buhler, E., Sartorelli, J., Represa, A., Baldelli, P., et al. (2019). TBC1D24 regulates axonal outgrowth and membrane trafficking at the growth cone in rodent and human neurons. *Cell Death Differ.* 26, 2464–2478. <https://doi.org/10.1038/s41418-019-0313-x>.
 25. Yim, W.W.Y., and Mizushima, N. (2020). Lysosome biology in autophagy. *Cell Discov.* 6, 6. <https://doi.org/10.1038/s41421-020-0141-7>.
 26. Decet, M., and Verstreken, P. (2021). Presynaptic Autophagy and the Connection With Neurotransmission. *Front. Cell Dev. Biol.* 9, 790721. <https://doi.org/10.3389/fcell.2021.790721>.
 27. Stavoe, A.K.H., and Holzbaur, E.L.F. (2019). Autophagy in Neurons. *Annu. Rev. Cell Dev. Biol.* 35, 477–500. <https://doi.org/10.1146/annurev-cellbio-100818-125242>.
 28. Tona, R., Chen, W., Nakano, Y., Reyes, L.D., Petralia, R.S., Wang, Y.X., Starost, M.F., Wafa, T.T., Morell, R.J., Cravedi, K.D., et al. (2019). The phenotypic landscape of a Tbc1d24 mutant mouse includes convulsive seizures resembling human early infantile epileptic encephalopathy. *Hum. Mol. Genet.* 28, 1530–1547. <https://doi.org/10.1093/hmg/ddy445>.
 29. Takamori, S., Holt, M., Stenius, K., Lemke, E.A., Grønborg, M., Riedel, D., Urlaub, H., Schenck, S., Brügger, B., Ringler, P., et al. (2006). Molecular anatomy of a trafficking organelle. *Cell* 127, 831–846. <https://doi.org/10.1016/j.cell.2006.10.030>.
 30. Hoffmann, S., Orlando, M., Andrzejak, E., Bruns, C., Trimbuch, T., Rosenmund, C., Garner, C.C., and Ackermann, F. (2019). Light-Activated ROS Production Induces Synaptic Autophagy. *J. Neurosci.* 39, 2163–2183. <https://doi.org/10.1523/JNEUROSCI.1317-18.2019>.
 31. Egashira, Y., Takase, M., Watanabe, S., Ishida, J., Fukamizu, A., Kaneko, R., Yanagawa, Y., and Takamori, S. (2016). Unique pH dynamics in GABAergic synaptic vesicles illuminates the mechanism and kinetics of GABA loading. *Proc. Natl. Acad. Sci. USA* 113, 10702–10707. <https://doi.org/10.1073/pnas.1604527113>.
 32. Gowrisankaran, S., and Milosevic, I. (2020). Regulation of synaptic vesicle acidification at the neuronal synapse. *IUBMB Life* 72, 568–576. <https://doi.org/10.1002/iub.2235>.
 33. Ivanova, D., and Cousin, M.A. (2022). Synaptic Vesicle Recycling and the Endolysosomal System: A Reappraisal of Form and Function. *Front. Synaptic Neurosci.* 14, 826098. <https://doi.org/10.3389/fnsyn.2022.826098>.
 34. Bott, L.C., Forouhan, M., Lieto, M., Sala, A.J., Ellerington, R., Johnson, J.O., Speciale, A.A., Criscuolo, C., Filla, A., Chitayat, D., et al. (2021). Variants in ATP6V0A1 cause progressive myoclonus epilepsy and developmental and epileptic encephalopathy. *Brain Commun.* 3, fcab245. <https://doi.org/10.1093/braincomms/fcab245>.
 35. Aoto, K., Kato, M., Akita, T., Nakashima, M., Mutoh, H., Akasaka, N., Tohyama, J., Nomura, Y., Hoshino, K., Ago, Y., et al. (2021). ATP6V0A1 encoding the $\alpha 1$ -subunit of the V0 domain of vacuolar H(+)-ATPases is essential for brain development in humans and mice. *Nat. Commun.* 12, 2107. <https://doi.org/10.1038/s41467-021-22389-5>.
 36. Hirose, T., Cabrera-Socorro, A., Chitayat, D., Lemonnier, T., Féraud, O., Cifuentes-Diaz, C., Gervasi, N., Mombereau, C., Ghosh, T., Stoica, L., et al. (2019). ATP6AP2 variant impairs CNS development and neuronal survival to cause fulminant neurodegeneration. *J. Clin. Invest.* 129, 2145–2162. <https://doi.org/10.1172/JCI79990>.
 37. Wilkens, S., Khan, M.M., Knight, K., and Oot, R.A. (2023). Tender love and disassembly: How a TLDc domain protein breaks the V-ATPase. *Bioessays* 45, e2200251. <https://doi.org/10.1002/bies.202200251>.
 38. Khan, M.M., Lee, S., Couoh-Cardel, S., Oot, R.A., Kim, H., Wilkens, S., and Roh, S.H. (2022). Oxidative stress protein Oxr1 promotes V-ATPase holoenzyme disassembly in catalytic activity-independent manner. *EMBO J.* 41, e109360. <https://doi.org/10.15252/emboj.2021109360>.
 39. Klössel, S., Zhu, Y., Amado, L., Bisinski, D.D., Ruta, J., Liu, F., and González Montoro, A. (2024). Yeast TLDc domain proteins regulate assembly state and subcellular localization of the V-ATPase. *EMBO J.* 43, 1870–1897. <https://doi.org/10.1038/s44318-024-00097-2>.
 40. Khan, M.M., and Wilkens, S. (2024). Molecular mechanism of Oxr1p mediated disassembly of yeast V-ATPase. *EMBO Rep.* 25, 2323–2347. <https://doi.org/10.1038/s44319-024-00126-5>.
 41. Wang, R., Qin, Y., Xie, X.S., and Li, X. (2022). Molecular basis of mEAK7-mediated human V-ATPase regulation. *Nat. Commun.* 13, 3272. <https://doi.org/10.1038/s41467-022-30899-z>.
 42. Tan, Y.Z., Abbas, Y.M., Wu, J.Z., Wu, D., Keon, K.A., Hesketh, G.G., Bueler, S.A., Gingras, A.-C., Robinson, C.V., Grinstein, S., and Rubinstein, J.L. (2022). CryoEM of endogenous mammalian V-ATPase interacting with the TLDc protein mEAK-7. *Life Sci. Alliance* 5, e202201527. <https://doi.org/10.26508/lsa.202201527>.
 43. Oot, R.A., and Wilkens, S. (2024). Human V-ATPase function is positively and negatively regulated by TLDc proteins. *Structure* 32, 989–1000.e6. <https://doi.org/10.1016/j.str.2024.03.009>.
 44. Castroflorio, E., den Hoed, J., Svistunova, D., Finelli, M.J., Cebrían-Serrano, A., Corrochano, S., Bassett, A.R., Davies, B., and Oliver, P.L. (2021). The Ncoa7 locus regulates V-ATPase formation and function, neurodevelopment and behaviour. *Cell. Mol. Life Sci.* 78, 3503–3524. <https://doi.org/10.1007/s00018-020-03721-6>.
 45. Finelli, M.J., Sanchez-Pulido, L., Liu, K.X., Davies, K.E., and Oliver, P.L. (2016). The Evolutionarily Conserved Tre2/Bub2/Cdc16 (TBC), Lysin Motif (LysM), Domain Catalytic (TLDc) Domain Is Neuroprotective against Oxidative Stress. *J. Biol. Chem.* 291, 2751–2763. <https://doi.org/10.1074/jbc.M115.685222>.
 46. Raghu, P., Joseph, A., Krishnan, H., Singh, P., and Saha, S. (2019). Phosphoinositides: Regulators of Nervous System Function in Health and Disease. *Front. Mol. Neurosci.* 12, 208. <https://doi.org/10.3389/fnmol.2019.00208>.
 47. Falace, A., Filipello, F., La Padula, V., Vanni, N., Madia, F., De Pietri Tonelli, D., de Falco, F.A., Striano, P., Dagna Bricarelli, F., Minetti, C., et al. (2010). TBC1D24, an ARF6-interacting protein, is mutated in familial infantile myoclonic epilepsy. *Am. J. Hum. Genet.* 87, 365–370. <https://doi.org/10.1016/j.ajhg.2010.07.020>.
 48. Tagliatti, E., Fadda, M., Falace, A., Benfenati, F., and Fassio, A. (2016). Arf6 regulates the cycling and the readily releasable pool of synaptic vesicles at hippocampal synapse. *Elife* 5, e10116. <https://doi.org/10.7554/eLife.10116>.
 49. Doyle, T., Moncorgé, O., Bonaventure, B., Pollpeter, D., Lussignol, M., Tauziet, M., Apolonia, L., Catanese, M.T., Goujon, C., and Malim, M.H. (2018). The interferon-inducible isoform of NCOA7 inhibits endosome-mediated viral entry. *Nat. Microbiol.* 3, 1369–1376. <https://doi.org/10.1038/s41564-018-0273-9>.
 50. Coupland, C.E., Karimi, R., Bueler, S.A., Liang, Y., Courbon, G.M., Di Trani, J.M., Wong, C.J., Saghian, R., Youn, J.Y., Wang, L.Y., and

- Rubinstein, J.L. (2024). High-resolution electron cryomicroscopy of V-ATPase in native synaptic vesicles. *Science* 385, 168–174. <https://doi.org/10.1126/science.adp5577>.
51. Fernandes, A.C., Uytterhoeven, V., Kuenen, S., Wang, Y.C., Slabbaert, J.R., Swerts, J., Kasprovicz, J., Aerts, S., and Verstreken, P. (2014). Reduced synaptic vesicle protein degradation at lysosomes curbs TBC1D24/sky-induced neurodegeneration. *J. Cell Biol.* 207, 453–462. <https://doi.org/10.1083/jcb.201406026>.
 52. Farias, G.G., Guardia, C.M., De Pace, R., Britt, D.J., and Bonifacio, J.S. (2017). BORC/kinesin-1 ensemble drives polarized transport of lysosomes into the axon. *Proc. Natl. Acad. Sci. USA* 114, E2955–E2964. <https://doi.org/10.1073/pnas.1616363114>.
 53. Vukoja, A., Rey, U., Petzoldt, A.G., Ott, C., Vollweiler, D., Quentin, C., Puchkov, D., Reynolds, E., Lehmann, M., Hohensee, S., et al. (2018). Pre-synaptic Biogenesis Requires Axonal Transport of Lysosome-Related Vesicles. *Neuron* 99, 1216–1232. <https://doi.org/10.1016/j.neuron.2018.08.004>.
 54. Einhorn, Z., Trapani, J.G., Liu, Q., and Nicolson, T. (2012). Rabconnectin3alpha promotes stable activity of the H⁺ pump on synaptic vesicles in hair cells. *J. Neurosci.* 32, 11144–11156. <https://doi.org/10.1523/JNEUROSCI.1705-12.2012>.
 55. Esposito, A., Falace, A., Wagner, M., Gal, M., Mei, D., Conti, V., Pisano, T., Aprile, D., Cerullo, M.S., De Fusco, A., et al. (2019). Biallelic DMXL2 mutations impair autophagy and cause Ohtahara syndrome with progressive course. *Brain* 142, 3876–3891. <https://doi.org/10.1093/brain/awz326>.
 56. Herman, M.A., Trimbuch, T., and Rosenmund, C. (2018). Differential pH Dynamics in Synaptic Vesicles From Intact Glutamatergic and GABAergic Synapses. *Front. Synaptic Neurosci.* 10, 44. <https://doi.org/10.3389/fnsyn.2018.00044>.
 57. Rost, B.R., Schneider, F., Grauel, M.K., Wozny, C., Bentz, C., Blessing, A., Rosenmund, T., Jentsch, T.J., Schmitz, D., Hegemann, P., and Rosenmund, C. (2015). Optogenetic acidification of synaptic vesicles and lysosomes. *Nat. Neurosci.* 18, 1845–1852. <https://doi.org/10.1038/nn.4161>.
 58. Lozano, R., Herman, K., Rothfuss, M., Rieger, H., Bayrak-Toydemir, P., Aprile, D., Fruscione, F., Zara, F., and Fassio, A. (2016). Clinical intrafamilial variability in lethal familial neonatal seizure disorder caused by TBC1D24 mutations. *Am. J. Med. Genet.* 170, 3207–3214. <https://doi.org/10.1002/ajmg.a.37933>.
 59. Guven, A., and Tolun, A. (2013). TBC1D24 truncating mutation resulting in severe neurodegeneration. *J. Med. Genet.* 50, 199–202. <https://doi.org/10.1136/jmedgenet-2012-101313>.
 60. Corbett, M.A., Bahlo, M., Jolly, L., Afawi, Z., Gardner, A.E., Oliver, K.L., Tan, S., Coffey, A., Mulley, J.C., Dibbens, L.M., et al. (2010). A focal epilepsy and intellectual disability syndrome is due to a mutation in TBC1D24. *Am. J. Hum. Genet.* 87, 371–375. <https://doi.org/10.1016/j.ajhg.2010.08.001>.
 61. Muona, M., Berkovic, S.F., Dibbens, L.M., Oliver, K.L., Maljevic, S., Bayly, M.A., Joensuu, T., Canafoglia, L., Franceschetti, S., Michelucci, R., et al. (2015). A recurrent *de novo* mutation in KCNC1 causes progressive myoclonus epilepsy. *Nat. Genet.* 47, 39–46. <https://doi.org/10.1038/ng.3144>.
 62. Yuan, Y., Zhang, J., Chang, Q., Zeng, J., Xin, F., Wang, J., Zhu, Q., Wu, J., Lu, J., Guo, W., et al. (2014). De novo mutation in ATP6V1B2 impairs lysosome acidification and causes dominant deafness-onychodystrophy syndrome. *Cell Res.* 24, 1370–1373. <https://doi.org/10.1038/cr.2014.77>.
 63. Versteegen, A.M.J., Tagliatti, E., Lignani, G., Marte, A., Stoloro, T., Atlas, M., Corradi, A., Valtorta, F., Gitler, D., Onofri, F., et al. (2014). Phosphorylation of synapsin I by cyclin-dependent kinase-5 sets the ratio between the resting and recycling pools of synaptic vesicles at hippocampal synapses. *J. Neurosci.* 34, 7266–7280. <https://doi.org/10.1523/JNEUROSCI.3973-13.2014>.
 64. Falace, A., Buhler, E., Fadda, M., Watrin, F., Lippiello, P., Pallesi-Pocachard, E., Baldelli, P., Benfenati, F., Zara, F., Represa, A., et al. (2014). TBC1D24 regulates neuronal migration and maturation through modulation of the ARF6-dependent pathway. *Proc. Natl. Acad. Sci. USA* 111, 2337–2342. <https://doi.org/10.1073/pnas.1316294111>.
 65. Schneider, C.A., Rasband, W.S., and Eliceiri, K.W. (2012). NIH Image to ImageJ: 25 years of image analysis. *Nat. Methods* 9, 671–675. <https://doi.org/10.1038/nmeth.2089>.
 66. Monaldi, I., Vassalli, M., Bachi, A., Giovedi, S., Millo, E., Valtorta, F., Raiteri, R., Benfenati, F., and Fassio, A. (2010). The highly conserved synapsin domain E mediates synapsin dimerization and phospholipid vesicle clustering. *Biochem. J.* 426, 55–64. <https://doi.org/10.1042/BJ20090762>.
 67. Chantranupong, L., Saulnier, J.L., Wang, W., Jones, D.R., Pacold, M.E., and Sabatini, B.L. (2020). Rapid purification and metabolomic profiling of synaptic vesicles from mammalian brain. *Elife* 9, e59699. <https://doi.org/10.7554/eLife.59699>.
 68. Burrinha, T., Cunha, C., Hall, M.J., Lopes-da-Silva, M., Seabra, M.C., and Guimas Almeida, C. (2023). Deacidification of endolysosomes by neuronal aging drives synapse loss. *Traffic* 24, 334–354. <https://doi.org/10.1111/tra.12889>.
 69. Cheville, N.F. (2013). Ultrastructural pathology and interorganelle cross talk in hepatotoxicity. *Toxicol. Pathol.* 41, 210–226. <https://doi.org/10.1177/0192623312467402>.
 70. Egashira, Y., Katsurabayashi, S., and Takamori, S. (2022). Quantitative Analysis of Presynaptic Vesicle Luminal pH in Cultured Neurons. *Methods Mol. Biol.* 2417, 45–58. https://doi.org/10.1007/978-1-0716-1916-2_4.
 71. Egashira, Y., Takase, M., and Takamori, S. (2015). Monitoring of vacuolar-type H⁺ ATPase-mediated proton influx into synaptic vesicles. *J. Neurosci.* 35, 3701–3710. <https://doi.org/10.1523/JNEUROSCI.4160-14.2015>.

STAR★METHODS

KEY RESOURCES TABLE

REAGENT or RESOURCE	SOURCE	IDENTIFIER
Antibodies		
Mouse monoclonal anti-Arf6; WB 1:1,000	Sigma-Aldrich	Cat#A5230; RRID:AB_2058488
Rabbit polyclonal anti-Atp6v0a1; WB 1:2,000	Novus	Cat#NBP1-89342; RRID:AB_11015740
Rabbit polyclonal anti-Atp6v1a; WB 1:1,000	Abcam	Cat#ab137574; RRID:AB_2722516
Rabbit polyclonal anti-Atp6v1a; WB 1:1,000	Proteintech	Cat#17115-1-AP; RRID:AB_2290195
Rabbit polyclonal anti-Atp6v1b2; WB 1:2,000	Abcam	Cat#ab73404; RRID:AB_1924799
Rabbit polyclonal anti-Atp6v1b2; WB 1:1,000	Proteintech	Cat#15097-1-AP; RRID:AB_2243297
Mouse monoclonal anti-tubulin beta III; ICC 1:200	Millipore	Cat#MAB1637; RRID:AB_2210524
Rabbit polyclonal anti-Flag; WB 1:1,000	Sigma-Aldrich	Cat#F7425; RRID:AB_439687
Rabbit monoclonal anti-Gapdh; WB 1:5,000	Cell Signaling	Cat#2118; RRID:AB_561053
Rabbit polyclonal anti-LC3B; WB 1:1,000 ICC 1:200	Sigma-Aldrich	Cat#L7543; RRID:AB_796155
Rabbit polyclonal anti-LC3B; WB 1:1,000	Novus	Cat#NB100-2220; RRID:AB_10003146
Mouse monoclonal anti-NaK3/ATP1A3; WB 1:2,000	Thermo Fisher Scientific	Cat#MA3-915; RRID:AB_2274447
Rabbit polyclonal anti-Lamp1; WB 1:1,000 ICC 1:200	Sigma-Aldrich	Cat#L1418; RRID:AB_477157
Rabbit polyclonal anti-Lamp1; WB 1:1,000	Abcam	Cat#ab24170; RRID:AB_775978
Mouse monoclonal anti-Map2; ICC 1:200	Sigma-Aldrich	Cat#M9942; RRID:AB_477256
Rabbit polyclonal anti-p62; WB 1:1,000 ICC 1:100	Sigma-Aldrich	Cat#P0067; RRID:AB_1841064
Rabbit monoclonal anti-Rab5; WB 1:1,000	Abcam	Cat#ab218624; RRID:AB_2892717
Mouse monoclonal anti-Rab7; WB 1:1,1000	Abcam	Cat#ab50533; RRID:AB_882241
Mouse monoclonal anti-Snap25; WB 1:500	Synaptic System	Cat#111011; RRID:AB_887794
Mouse monoclonal anti-synaptophysin1; WB 1:1,000	Synaptic System	Cat#101011; RRID:AB_887824
Rabbit polyclonal anti-Tbc1d24; WB 1:1,000	Novus	Cat#NBP1-82925; RRID:AB_11061868
Rabbit polyclonal anti-Tbc1d24; WB 1:500	This paper	N/A
Rabbit polyclonal anti-Vamp2; WB 1:5,000	Synaptic System	Cat#104202; RRID:AB_887810
Goat Anti-Rabbit IgG (H + L)-HRP Conjugate; WB 1:3,000	BioRad	Cat#170-6515; RRID:AB_11125142
Goat Anti-Mouse IgG (H+L)-HRP Conjugate; WB 1:5,000	BioRad	Cat#170-6516; RRID:AB_2921252
EasyBlot anti Rabbit IgG (HRP); WB 1:1,000	Genetex	Cat#GTX221666-01; RRID:AB_10620421
Goat anti-Mouse IgG (H+L) Highly Cross-Adsorbed Secondary Antibody, Alexa Fluor 488	Thermo Fisher Scientific	Cat#A11029;RRID:AB_2534088
Goat anti-Guinea Pig IgG (H+L) Highly Cross-Adsorbed Secondary Antibody, Alexa Fluor 647	Thermo Fisher Scientific	Cat#A21450;RRID:AB_2535867
Bacterial and virus strains		
Lentivirus expressing synaptophysin-pHluorin	Verstegen A.M.J et al. ⁶³	N/A
Lentivirus expressing syp-mCherry and LC3-eGFP	Hoffmann, S et al. ³⁰	N/A
Chemicals, peptides, and recombinant proteins		
Bafilomycin A1	Merck	Cat#19-148
CNQX	Tocris	Cat#1045
D-APV	Tocris	Cat#0106
FCCP	Tocris	Cat#0453
Nigericin	Tocris	Cat#4312
Valinomycin	Tocris	Cat#3373
Protease inhibitor cocktail	Cell Signaling	Cat#5871

(Continued on next page)

Continued		
REAGENT or RESOURCE	SOURCE	IDENTIFIER
Protease inhibitors – complete EDTA free	Roche	Cat#COEDTAF-RO
Protein G Sepharose beads	Sigma Aldrich	Cat# GE17-0618-01
Phosphatase inhibitor cocktail	Cell signaling	Cat#5870
Lysotracker	Thermo Fisher Scientific	Cat#L12492
LysoSensor Yellow/Blue DND-160	Thermo Fisher Scientific	Cat#L7545
Critical commercial assays		
anti-Flag M2 Affinity Gel	Sigma-Aldrich	Cat#A2220
Arf6 Activation Assay Biochem Kit	Cytoskeleton	Cat#BK033-S
Experimental models: Cell lines		
COS-7	ATCC	ATCC-CRL-1651
Experimental models: Organisms/strains		
Mouse: C57BL/6J	Charles River	C57BL/6J
Mouse: C57BL/6J-Tbc1d24 ^{INS+/-}	This paper	N/A
Rat: Sprague Dawley	Charles River	CD® IGS
Oligonucleotides		
FW primer Tbc1d24 genotyping 5'-GCCTGAGTTTGTAGACAACAC-3'	This paper	N/A
REV primer Tbc1d24 genotyping 5'-CCCAAATGTCATACAGGAAG-3'	This paper	N/A
Recombinant DNA		
TBC1D24-pCAGG	Falace, A et al. ⁶⁴	N/A
Nterm-3XFLAG-TBC1D24	This paper	N/A
p3XFLAG-CMV-10	Sigma-Aldrich	Cat#E7658
pmCherry-1	Clontech	Cat#632524
pEGFP-C1	Falace, A et al. ⁴⁷	N/A
TBC1D24-mCherry	This paper	N/A
mU6pro	Falace, A et al. ⁶⁴	N/A
pLKO.3G	Addgene	Cat#14748; RRID:Addgene14748
Human ATP6V1B2-HA	Philippe Campeau	N/A
ATP6V1B2-FLAG	Philippe Campeau	N/A
ATP6V1A-FLAG	Philippe Campeau	N/A
human ATP6V1A pLVX-IRES-mCherry	Fassio, A et al. ⁸	N/A
human ATP6V1B2-GFP	Philippe Campeau	N/A
pEGFP-N1	Clontech	N/A
FU-Syp-mCherry-P2A-eGFP-LC3	Hoffmann, S et al. ³⁰	N/A
pCCLsin.PPT.hPGK.deltanGFRpre-Syphy	Verstegen A.M.J et al. ⁶³	N/A
Software and algorithms		
ImageJ	Schneider CA et al. ⁶⁵	https://imagej.net/ij/
ImageLab	Bio-Rad	https://www.bio-rad.com/it-it/product/image-lab-software
MATLAB Version: 9.9.0.1718557 (R2020b)	MATLAB. (2020b). Natick, Massachusetts: The MathWorks Inc.	https://it.mathworks.com
GraphPad Prism 8.4.2	GraphPad Software, San Diego, California, USA	www.graphpad.com

EXPERIMENTAL MODEL AND STUDY PARTICIPANT DETAILS

Tbc1d24 null mouse model

In the process of targeting the endogenous *Tbc1d24* gene by CRISPR-Cas9 (MRC Harwell), mice bearing a two nucleotide (CG) insertion in exon 3 (ENSMUSE00000475486) were generated by non-homologous end joining (NHEJ), causing a predicted frame-

shift and premature stop codon (p.Val137Alafs*45). A sgRNA (sequence 5'- AGTAGCAAGGCCACCACAGC-3') targeting *Tbc1d24* exon 3 was synthesized *in vitro*. Cas9 mRNA, sgRNAs and donor DNA (sequence ssODNs 5'- TGTGCGCAAGATCCTCCTGTGTATTGCCAACAGTCCCTGACATCTCCTTCTGCCCTGCCCTGCTTGCAGTCGTGGCCTTGCTACTGCACTACAGCATCG ATGAAGCTGAGTGTTCGAAAAAGCCTGCCGC-3') were microinjected into the pronucleus of fertilized one-cell embryos of C57BL/6J mice. The injected one-cell embryos were transferred into the pseudo pregnant female mice. Host females were allowed to litter and rear F0 progeny.

The presence of genomic modification in the F0 generation was determined by genomic DNA analysis via PCR and Sanger sequencing on ear clip samples. F0 generation mice were mated with WT C57BL/6J mice of the same age to obtain F1 generation mice. These mice underwent PCR and Sanger sequencing to enable definite characterization of the mutant allele. Animals that showed the desired base changes also underwent copy counting analysis via digital droplet PCR to check against additional donor integrations in the genome (Forward primer sequence 5'-TGTGCGCAAGATCCTCCTG-3', Reverse Primer sequence 5'-CAAGGC CACGACTGCAA-3', Probe sequence 5'-TGTATTGCCAACAGTCCCTGACA-3'). No additional donor insertions were detected in the animals taken forward to establish the colony. In addition, a potential off-target site with 2 mismatches was sequenced, with no evidence of off-target guide activity was identified.

Subsequently, mature F1 generation mice were backcrossed to obtain F2 generation *Tbc1d24*^{INS2/+} mice (HET) and F2 generation were inter-crossed to obtain homozygous *Tbc1d24*^{INS2/INS2} mice (KO). All F2 embryos were genotyped by qPCR. In addition, a potential off-target site on Chromosome 2 (AGAAGCAAGGCCACCACAGG) with 2 mismatches was sequenced, with no evidence of off-target guide activity was identified (Forward primer sequence 5'- TCTCTGGGACCCACATAGGG-3', Reverse primer 5'-CACAGTGTGAAAAGCTGGC-3').

Whilst F0 and F1 samples were genotyped by PCR and sequencing, F2 offspring and subsequent generations were genotyped by qPCR. Mouse ear DNA was extracted using the DNA Extract All Reagents Kit (Thermo Fisher Scientific) and stored at -20°C until use. Samples were genotyped using qPCR with a FAM-labelled TaqMan assay (LGC, Biosearch Technologies, 5 μM probe, 15 μM each primer) designed to detect either the WT *Tbc1d24* allele or the mutant *Tbc1d24* allele, run in multiplex with a VIC-labelled internal control Dot1L (Thermo Fisher Scientific, 5 μM probe, 20 μM each primer), TaqMan GTXpress Master Mix (Thermo Fisher Scientific) and 1:10 dilution of DNA Extract All Reagents Kit preparation. Alternatively, genotyping was carried out by amplification of a 279 bp region flanking the mutation from genomic DNA with primers 5'-GCCTGAGTTGTAGACAACAC-3' and 5'-CCCAAATGTCATACAG GAAG-3'. PCR products were purified (Qiagen PCR clean-up) and digested with the BseXI enzyme and separated by agarose gel electrophoresis. The mutant allele is digested into two products of 118 and 161 bp.

Ethical statement for animal experiments

All experimental procedures conducted on animals were carried out so in accordance with the Animals (Scientific Procedures) Act 1986 Amendment Regulations 2012 (SI 4 2012/3039) at Harwell (Didcot, UK). Mice were housed in Tecniplast IVC cages (1284L and 1285L) with Aspen bedding (Datesand). Food and water were provided *ad libitum*. The lighting regime was 12 hr light, 12 hr dark with 30 min dusk to dawn, dawn to dusk period. Health checks were conducted daily and a maximum number of five animals were housed per cage.

Mouse and rat primary cultures

Mouse primary neurons were prepared from embryos at E15-16 and each embryo was treated independently. Rat primary hippocampal neurons were prepared from pulled embryos at E18. Cortices and hippocampi were dissected under a stereomicroscope in ice-cold HBSS. Cortices and hippocampi were incubated for 10-15 min in 0.25% trypsin (Gibco) at 37°C. Trypsin was replaced with Neurobasal medium (1X, Gibco) supplemented with 10% Fetal Bovine Serum (FBS, Gibco), 1% GlutaMAX (Gibco) and 1% Penicillin/Streptomycin (PenStrep, Gibco). The digested tissues were mechanically dissociated, cells were counted and plated on Petri dishes and 25 mm coverslips coated with Poly-L-Lysine (0.1 mg/mL for Petri and 1 mg/mL for coverslips) at a density of 200 cells/mm². 2 hr from plating, the medium was replaced with Neurobasal medium supplemented with B27 (1X, Gibco), 1% GlutaMAX and 1% PenStrep (hereby, complete Neurobasal medium). Cultures were maintained in a 5% CO₂ humidified incubator at 37°C for the indicated days *in vitro* (DIV). The sex of each embryonic animal was not determined; however multiple replicates will represent both males and females.

COS-7 cell culture

COS-7 cells were grown in Advanced DMEM (Life Technologies) supplemented with 10% FBS, 1% GlutaMAX (Gibco) and 1% PenStrep (Gibco) (hereby, complete A-DMEM medium) in a 5% CO₂ humidified incubator at 37°C. Cells were not authenticated or tested for mycoplasma contamination.

Custom antibody production

A peptide corresponding to amino acid residues 447-463 of mouse *Tbc1d24* was synthesized and used to immunize rabbits (Covablab, France). Antisera were affinity purified on Sulfolink coupling gel (Pierce) according to the manufacturer's recommendations. Activity of the antibody was confirmed by Western blotting (1:500) to mouse brain tissue and a mouse *Tbc1d24* clone expressed in HEK293T cells (Figure S1C).

METHOD DETAILS

Embryo histology and *in situ* hybridisation

The *Tbc1d24* transcript was detected on frozen tissue sections cut at 14 μm using a DIG-labelled probe as previously described.⁴⁵ For representative histopathology, frozen sections were stained with Cresyl Violet.

Constructs

TBC1D24-pCAGG construct expressing the full length human TBC1D24 was previously described.⁶⁴ Nterm-3XFlag-TBC1D24 (FLAG-TBC1D24) construct was obtained by subcloning human TBC1D24 sequence from the TBC1D24-pCAGG vector into p3XFLAG-CMV-10 (Sigma-Aldrich, #E7658) linearized with EcoRI and KpnI (NEB). Nterm-3XFlag-bacterial alkaline phosphatase (FLAG-BAP) was included in the p3XFLAG-CMV-10 kit (Sigma-Aldrich, #E7658). TBC1D24-mCherry was obtained by subcloning the human TBC1D24 sequence from pEGFP-C144 in pmCherry-1 (Clontech) linearized by BglII and Sall (NEB).

To acutely knockdown the *Tbc1d24* expression in rat primary neurons, short-hairpin RNAs (shRNAs) sequences either for silencing and scrambled control (respectively named Sh-TBC and Scr-TBC) were subcloned from mU6pro vector⁶⁴ and inserted in pLKO.3G lentiviral vector (Origene, Rockville, USA). Briefly, pLKO.3G was linearized after digestion with PacI and EcoRI (NEB). Annealing of shRNA sequences was performed with 100 nmoles/mL per oligonucleotide sequence in annealing buffer (100 μM NaCl, 10 mM Tris pH 7.4). Ligation of linearized pLKO.3G and oligos was performed with T4 Ligase (NEB) at room temperature for 2.5 hr.

Human ATP6V1B2-HA and ATP6V1B2-FLAG and ATP6V1A-FLAG tagged constructs were kindly gifted by Philippe Campeau (Montreal, Canada). The human ATP6V1A pLVX-IRES-mCherry was purchased from Biomatik (Biomatik Corporation, Kitchener, Ontario, Canada). The human ATP6V1B2-GFP was generated by RT-PCR and subcloned into pEGFP-N1 (Clontech). The lentiviral construct FU-Syp-mCherry-P2A-eGFP-LC3 was kindly provided by Craig Garner³⁰ and pCCLsin.PPT.hPGK.deltaNGFRpre-Syphy was previously described.⁶³

Cell transfection

COS7 cells

The day before transfection, 3×10^6 cells were plated on 60 mm Petri dishes in complete A-DMEM medium. The medium was replaced with Advanced DMEM 1 hr before adding transfection reagent prepared as follows: 4 μL of polyethyleneimine (PEI) were diluted in 36 μL of water and mixed with 6 μg of cDNA in 200 μL of Advanced DMEM for 10 min. The transfection reagent was added for 1.5 hr and replaced with complete fresh A-DMEM medium.

Primary neurons

Transfection of primary neurons was performed with Lipofectamine 2000 (Thermo Fisher Scientific) following manufacture's instructions with minor modifications. For each coverslip, the transfection reagent was prepared as follows: 1 μL Lipofectamine diluted in 45 μL of Neurobasal medium and incubated for 5 min at room temperature. 0.1 μg of cDNA was diluted in 45 μL of Neurobasal medium and mixed with the Lipofectamine for 20 min. Immediately before transfection, the conditioned Neurobasal medium was removed from cells, stored and replaced with 210 μL /well of fresh Neurobasal medium. Transfection reagent was added for 30 min and replaced with 2 mL of conditioned Neurobasal medium. Experiments were performed 2-3 days after transfection.

Cell transduction

Transduction of primary neurons was performed at 14 DIV. 800 μL of the conditioned medium was collected from each well, mixed with equal volume of complete Neurobasal medium and stored at 4°C (conditioned medium). Viral particles were diluted in 400 μL well of complete Neurobasal medium and incubated for 18-20 hr. The infection medium was removed and replaced with the conditioned one. Experiments were performed 3-5 days after transduction.

Pull-down

For pull-down experiments of endogenous Atp6v1a and Atp6v1b2, FLAG-TBC1D24, FLAG-BAP, empty p3XFLAG-CMV-10 Expression Vector (FLAG) were transfected in COS-7 cells and purified by anti-Flag M2 Affinity Gel. For pull down experiments of exogenous proteins: FLAG-TBC1D24 and FLAG-BAP were cotransfected in COS-7 cells, with ATP6V1B2-HA or ATP6V1A and ATP6V1A-FLAG, ATP6V1B2-FLAG or FLAG BAP were cotransfected with TBC1D24-pCAGG. 24 hr after transfection, cells were harvested in lysis buffer (150 mM NaCl, 1% Triton, 50 mM Tris, 1 mM EDTA pH 8.0) supplemented with protease inhibitors and centrifuged at 10,000 $\times g$ for 10 min at 4°C. An aliquot was reserved for input and the supernatant was incubated with anti-FLAG M2 Affinity Gel following the manufacturer's guidelines. Pulled down proteins together with aliquots of the input material were analysed by Western blotting.

Immunoprecipitation from brain tissue

Tissue was homogenised in lysis buffer (150 mM NaCl, 1% NP40, 0.5% DOC and 50 mM Tris pH 7.5) containing protease inhibitors (complete - EDTA free) and centrifuged for 30 min at 16000 $\times g$ at 4°C. 5 mg lysates were precleared using protein-G Sepharose beads, incubated with custom anti-Tbc1d24 antibody overnight at 4°C, followed by incubation with protein-G Sepharose beads

for 2 hr at 4°C. Bound proteins were eluted from the beads by adding 60 µl LDS sample buffer containing 50 mM DTT and heating at 95°C for 5 min. Eluted proteins were analysed by Western blotting.

Cytosol/membrane fractionation

Cortical neurons at 12 DIV were placed on ice, washed with phosphate buffered saline (PBS) and scraped into homogenization buffer (250 mM sucrose, 1 mM EDTA pH 8.0) supplemented with protease and phosphatase inhibitor cocktails. Samples were collected, homogenized 8-10 times through a 29 g syringe needle and centrifuged at 500 x g for 10 min at 4°C. The supernatants were collected and ultracentrifuged at 100,000 x g for 30 min at 4°C. The supernatants were collected, quantified and stored at -20°C (cytosolic fraction). The pellet was rinsed, resuspended with the homogenization buffer, quantified and stored at -20°C (membrane fraction). The fractions were then separated by SDS-PAGE. The quality of subcellular fractionation was evaluated by Western blotting using anti-Vinculin (cytosolic marker) and anti-NaK3 (membrane marker).

Synaptosomes from rat brain and primary neurons

Purified synaptosomes from rat brain were prepared as previously described.⁶⁶ Three-month old rat cerebral cortex was homogenized in ice-cold HB buffer (0.32 M sucrose, 1 mM EDTA, 10 mM Tris, pH 7.4) containing protease inhibitors (2 mg/mL pepstatin, 0.2 M PMSF) using a glass-Teflon homogenizer. The homogenate was centrifuged at 1,000 x g for 5 min at 4°C to remove nuclei and debris, and the supernatant (H) was further centrifuged at 18,900 x g for 5 min at 4°C to obtain the crude synaptosomal fraction (Syn). The Syn was resuspended in 2 mL of HB buffer and gently stratified on a discontinuous Percoll gradient (2, 6, 10 and 20% (v/v) in HB buffer). After 10 min of centrifugation at 33,500 x g at 4°C, the purified synaptosomal fraction (pSyn) was collected from the 10 to 20% Percoll interface and washed by centrifugation (20,000 x g for 5 min at 4°C) to eliminate Percoll. Ultrasynaptic fractionation was performed as previously described.⁴⁸ Briefly, synaptosomes were pelleted and resuspended in 300 ml of 0.32 M sucrose, 0.1 mM CaCl₂, diluted 1:10 in ice-cold .1 mM CaCl₂ and mixed with an equal volume of 2X solubilization buffer (2% Triton X-100, 40 mM Tris, pH 6, 4°C). After a 30 min incubation at 4°C, the insoluble material (synaptic junction) was pelleted by centrifugation (40,000 X g, 30 min, 4°C). The supernatant (1% TX-100 pH 6 soluble) was decanted, and the proteins precipitated with 6 volumes of acetone at -20°C overnight and then centrifuged (18,000 x g, 30 min, -15°C). The synaptic junction pellet (containing the insoluble postsynaptic density and the presynaptic membrane) was resuspended in 10 volumes of 1X solubilization buffer (1% Triton X-100, 20 mM Tris, pH 8, 4°C), incubated for 30 min at 4°C and then centrifuged (40,000 x g, 30 min, 4°C). The proteins in the supernatant (1% TX-100 pH 8 soluble) were precipitated in 6 volumes of acetone at -20°C overnight and then centrifuged (18,000 x g, 30 min, -15°C), while the pellet was kept as postsynaptic density fraction (1% TX-100 pH 8 insoluble). All pellets were resuspended in 5% SDS, quantified by BCA assay, and loaded on SDS-PAGE gels for electrophoresis and consecutive western blotting.

Synaptosomes from primary neurons were prepared accordingly to Chantranupong et al.⁶⁷ Briefly, cortical neurons at 15 DIV were washed twice with ice-cold PBS to remove residual media and gently scraped into 1 mL PBS. After a centrifugation step at 2,400 x g for 40 s, the pellet was resuspended in 1 mL of homogenization buffer (320 mM sucrose, 4 mM HEPES NaOH, pH 7.4) supplemented with protease inhibitors and 1 mM ATP NaOH, pH 7.4. Cells were homogenized with 25 steady strokes and centrifuged at 2,400 x g for 40 s to pellet unbroken cells. The supernatant was then transferred to a new tube and centrifuged at 14,000 x g for 3 min to pellet crude synaptosomes (Syn).

Arf6 activation state evaluation

Arf6 activation state was determined using a commercial kit for specific pulldown of Arf6-GTP, according to manufacturer's instructions. Total lysates and pulled-down fractions were then separated by SDS-PAGE and the levels of Arf6-GTP and total Arf6 were evaluated by Western blotting.

Western blotting

Tissue lysates and their respective immunoprecipitates were separated on 4-12% NuPage gel (Thermo Fisher Scientific) and proteins transferred onto a nitrocellulose membrane using iBlot gel transfer stacks (Thermo Fisher Scientific). Cellular lysates, pulldown samples and subcellular fractions were separated on 8-12% polyacrylamide gel and proteins transferred onto a 0.2 µm nitrocellulose membrane (Amersham, #10600001) in Transfer Buffer (25 mM Tris HCl, 190 mM glycine pH 8.3, 20% methanol) for 2.5 hr at 350 mA or overnight at 40 mA at 4°C. Membranes were blocked in 1X Tris buffered Saline (TBS, BIO-RAD) containing 0.1% TWEEN 20 (Fisher Bioreagents) and 5% skimmed milk (Sigma-Aldrich) for 1 hr at room temperature, before incubation with primary antibodies 3 hr at room temperature or overnight at 4°C with constant agitation. Membranes were washed 3 times with TBS-Tween before incubating for 1 hr using goat-anti-rabbit-HRP secondary antibody (Sigma-Aldrich) at 1:10,000, Easy blot anti-rabbit-HRP GTX22166-01 (Genetex) at 1:1,000 or goat anti-rabbit HRP conjugate 1:3,000 (BioRad, #170-6515), goat anti-mouse HRP conjugate 1:5,000 (BioRad, #170-6516). Membranes were washed 3 times with TBS-Tween and protein bands visualised by chemiluminescence using Covalight Plus ECL reagent (Covalab, France), Pierce Super Signal West Pico PLUS Chemiluminescent Substrate (Thermo Fisher Scientific) or ECL reagent (Biorad, #170-5061). Protein signals were acquired using Chemidoc (BioRad) and the densitometric analysis of immunoreactive bands was performed with the ImageLab software.

Electron microscopy

Cultured neurons

Cortical neurons were fixed at 14–18 DIV with 1.2% glutaraldehyde in 66 mM sodium cacodylate buffer, post-fixed in 1% OsO₄, 1.5% K₄Fe(CN)₆, 0.1 M sodium cacodylate, *en bloc* stained with 1% uranyl acetate, dehydrated and flat-embedded in epoxy resin (Epon 812, TAAB). After baking for 48 hr, the glass coverslips were removed from the Epon block by thermal shock and neurons were identified by means of a stereomicroscope. Embedded neurons were excised from the block, and mounted on a cured Epon block for sectioning using an EM UC6 ultramicrotome (Leica Microsystems). Ultrathin sections (60–70 nm thick) were collected on 200-mesh copper grids (Electron Microscopy Sciences) and observed with a JEM-1011 electron microscope (Jeol) operating at 100 kV using an ORIUS SC1000 CCD camera (Gatan, Pleasanton). For each experimental condition, at least 30 images of synapses were acquired at 10,000x magnification (sampled area per experimental condition: 36 μm²). Synaptic profile area, SV number and distribution relative to the active zone (AZ) were determined using ImageJ software.

For the 3D reconstruction, the standard TEM sample preparation protocol was followed, and samples were embedded in Epon resin. Serial 60-nm-thick sections were collected on carbon-coated copper slot formvar and carbon-coated grids, and serial synaptic profiles acquired. Serial sections were aligned using Midas from IMOD software. Synapses with one single AZ, at least one docked SV and greater than 100 SVs were reconstructed with IMOD software.

Embryonic tissue

Brains were removed and fixed in 2.5% glutaraldehyde / 2% PFA in 0.1M sodium cacodylate buffer. Samples were then loaded into a Leica EM AMW automated microwave processing unit and processed into resin. In the AMW, samples were washed 4 times with 0.1M sodium cacodylate buffer, including one round with 50mM glycine to block free aldehydes. The samples were then stained with 1% osmium tetroxide with 1.5% potassium ferrocyanide, washed with water, stained with 2% uranyl acetate, then taken through an ethanol dehydration series and infiltrated with low viscosity epoxy resin (TAAB Laboratories). Samples were removed from the AMW and then given an additional overnight incubation in fresh resin with rotation at room temperature. Samples were embedded in beam capsules and polymerised for 48 hr at 60°C. Ultrathin sections (90 nm) were obtained using a Diatome diamond knife on a Leica EM UC ultramicrotome and transferred to 200 mesh copper grids. Sections were stained for 5 min with Reynold's lead citrate. Images were acquired using a FEI Tecnai T12 TEM operated at 120 kV and an OneView CMOS camera (Gatan). Lysosome and lipid droplets were identified as electron dense intracellular compartment of dark composition and clear round vesicle with jagged edge as previously described.^{68,69}

LysoTracker and Lysosensor experiments

LysoTracker (LTR)

Neurons were incubated with 100 nM LTR for 30 min in the incubator, fixed in 4% paraformaldehyde (PFA) + 4% sucrose in PBS for 15 min at room temperature and mounted with ProLong Gold Antifade Mountant with DAPI (Thermo Fisher Scientific, #P36935). Samples were acquired within 12 hr to prevent LTR signal decay. Images were taken with a confocal microscope (SP8, Leica) using 63x oil-immersion objective.

Lysosensor

Neurons were incubated for 3 min with 10 μM LysoSensor Yellow/Blue DND-160 in the incubator. Cells were then washed in Tyrode's solution (140 mM NaCl, 2.5 mM KCl, 10 mM HEPES pH 7.4, 10 mM glucose, 2 mM CaCl₂, 1 mM MgCl₂, pH 7.4) and live imaged with double excitation at 340 ± 10 nm or 380 ± 10 nm and single emission using a 400 nm long-pass filter on an epifluorescence microscope (Olympus 1X81, 60x oil-immersion objective). LysoSensor ratios (340/380 nm) were calculated from background subtracted images.

Immunocytochemistry

Neurons (12–18 DIV) were fixed in 4% paraformaldehyde (PFA) + 4% sucrose in PBS for 15 min at room temperature, permeabilized with 0.1% Triton X-100 (Sigma-Aldrich) in PBS for 10 min and incubated with blocking solution (5% FBS in PBS) for 30 min. Primary antibodies were diluted in blocking solution and incubated for 1 hr at room temperature or overnight at 4°C. Secondary antibodies were diluted 1:500 in blocking solution and incubated for 45 min at room temperature. Z-stack images of neurons were taken with a confocal microscope (SP8, Leica) using 63x oil-immersion objective. Settings were kept constant for all acquisitions within each experiment.

For colocalization experiments, Pearson's and Mander's coefficients were calculated in each focal plane in total cell area using the plugin JACoP of ImageJ software.

Live-imaging phluorin experiments

Neurons were transduced as described above with synaptophysin-phluorin (sypHy) lentiviral particles. Fluorescence imaging was performed on a wide-field inverted epifluorescence microscope (Olympus IX81) with a 60x oil-immersion objective, and a broad-spectrum LED illumination (pE-300ultra, CoolLED) was used. The filter set for sypHy consisted of 480 ± 20 nm excitation filter, 495 nm dichroic mirror, and 525 ± 50 nm emission filter. Images were captured at 1 frame/s at a depth of 12-bits using an Orca C4742-80-12AG CCD camera (Hamamatsu Photonics). The Tyrode's solution was supplemented with 25 μM CNQX, and 50 μM D-APV to block glutamatergic transmission. For the KCl stimulation, a modified Tyrode's solution in which 50 mM NaCl was replaced by 50 mM KCl was used. For the acidic quench, 10 mM HEPES was replaced with 10 mM MES and the pH of the solution was

equilibrated to 5.5. For the NH₄Cl challenge, a modified Tyrode's solution in which 50 mM NaCl was replaced by 50 mM NH₄Cl was used. Coverslips were mounted into the imaging chamber (Quick Exchange Platform, Warner Instruments). Cells were perfused with the different buffers at room temperature using laminar flow perfusion. Vacuum suction was applied to the opposite site of the chamber to stabilize the chamber volume.

Calibration of pHluorin probe

To estimate the pKa and Hill's coefficient (nH) of sypHy *in situ*, calibration experiments were performed accordingly to the protocol described by Egashira and colleagues.⁷⁰ Briefly, neurons transduced with sypHy were incubated for 1 min with Tyrode's solution supplemented with a cocktail of ionophores (20 μM FCCP, 10 μM valinomycin, 10 μM nigericin, 2 μM bafilomycin A1 and 0.02% Triton-X 100) to equilibrate the vesicular pH to extracellular pH. Neurons were washed for 15 sec with Tyrode's in continuous perfusion and then incubated (15 sec for each step) with K⁺-rich solutions clamped at 7 different pH value (122.4mM KCl, 20 mM NaCl, 10 mM HEPES for pH ≥ 6.8 or MES for pH ≤ 6.2, 10 mM glucose, 2 mM CaCl₂, and 1 mM MgCl₂; pH 8.5, 8.0, 7.4, 6.8, 6.2, 5.6, 5.0) in stop flow. Washing steps of 15 sec with Tyrode's solution were performed between one pH step and another and cells were imaged for 15 sec during K⁺-rich solution incubation. Images were acquired as above. The fluorescence intensity was obtained by averaging the 15 seconds of recording for each condition.

QUANTIFICATION AND STATISTICAL ANALYSIS

Imaging analysis

Colocalization

Z-stack images of neurons were taken with a confocal microscope (SP8, Leica) using 63x oil-immersion objective. Settings were kept constants for all acquisitions within each experiment. Pearson's and Mander's coefficients were calculated in each focal plane in total cell area using the plugin JACoP of ImageJ software.

Synaptic autophagy evaluation

Neurons were infected with FU-Syp-mCherry-P2A-eGFP-LC3 lentivirus and analysed after fixation. Z-stacks of neurons were taken as above. The counting of synapses positive for LC3 was performed by colocalization analysis between syp-mCherry and eGFP-LC3 signals. Colocalization puncta with areas of 0.1-2 μm² were considered *bona fide* synapses. To evaluate the abundance of LC3 within synaptic terminals, ROIs of 2 μm² were drawn on random syp-mCherry positive puncta and the average fluorescence intensity of eGFP-LC3 was measured.

SV pH measurements

To determine the pKa and Hill's coefficient (nH) values, ROIs of about 2 μm² were drawn on sypHy positive puncta, fluorescent intensities at each pH were measured after background subtraction and normalized to those at pH 8.5. Then, fluorescence values were fitted using the least square method (Matlab software) to the following equation⁷¹:

$$F / F_{pH8.5} = A + B / \left(1 + 10^{nH \times (pKa - pH)} \right)$$

where pKa is the pH at which 50% of the probe molecules are protonated, and nH is the Hill coefficient, which is proportional to slope of the fitting curve at pKa. pKa was measured as 6.85 and the nH value was measured as 0.99.

Calculations of the SV pH and the other related parameters was made as described previously by Egashira and colleagues.^{70,71} To evaluate the Surface fraction (S) and the pH before and after the stimulation with KCl, F_{0_pre}, F_{0_post}, F_{Q_pre}, F_{Q_post} and F_{max} were calculated. Specifically, F_{0_pre} and F_{0_post} represent the average fluorescence values over the last 10 seconds of the basal recording before acidic quench, prior to and following stimulation, respectively. F_{Q_pre} and F_{Q_post} were derived by averaging the last 10 seconds during acidic quench before and after stimulation or by fitting with single exponential decay the 15 seconds of the acidic quench before and after stimulation. F_{max} was determined by averaging the fluorescence during a 10 second application of ammonium-rich solution. Surface fraction was calculated as:

$$S = \frac{\frac{F_0}{F_{max}} - \frac{F_{mes}}{F_{max}}}{1 - \frac{F_{pH5.5}}{F_{pH7.4}}}$$

where

$$\frac{F_{pH5.5}}{F_{pH7.4}} = \frac{1}{1 + 10^{nH \times (pKa - 5.5)}} \bigg/ \frac{1}{1 + 10^{nH \times (pKa - 7.4)}}$$

SV pH was determined using the following equation:

$$\text{pH}_v = \text{pKa} - \frac{\log\left(\frac{1 + 10^{n\text{H}(\text{pKa} - 7.4)}}{\frac{F_{\text{pH}_v}}{F_{\text{max}}} - 1}\right)}{n\text{H}}$$

where

$$\frac{F_{\text{pH}_v}}{F_{\text{max}}} = \frac{F_0}{1 - S}$$

To estimate SV endocytosis and reacidification the Area Under the Curve (AUC) was evaluated during the recovery period, after KCl stimulation. To evaluate the release of the SV during stimulation we evaluated the $\Delta F_{\text{peak}}/F_{\text{max}}$. Briefly, Δ_{peak} is defined as the fluorescence at the peak (F_{peak}) during the stimulation minus the fluorescence recorded immediately before the stimulus (F_0). F_{peak} is determined by averaging the fluorescence over the 3 second in which it was highest during the stimulation, while F_0 is the average fluorescence from a 5-second recording before the stimulus.

Statistical analysis

The statistical analysis was performed with GraphPad Prism 6 software, and it is described in the figure legends. Data are expressed as box plots (centre line, median [Q2]; box limits, 25th [Q1]-75th [Q3] percentiles; whisker length, the outermost data points within 3-fold the interquartile range [Q3-Q1]) or as bar blots (means \pm SEM). All data were tested for outliers (ROUT test) and for normal distribution (D'Agostino-Pearson's test for $n \geq 8$) before performing statistical tests. Data with normal distribution were analysed by the unpaired Student's t-test; non-normally distributed data were analysed by the Mann-Whitney's U-test. Statistical significance between more than two normally distributed groups was evaluated using one-way ANOVA multiple comparisons test. Statistical test employed and number of samples are indicated for all data in the respective figure legends. Significance level was preset to $p < 0.05$.